

Environmental factors influencing the seasonal dynamics of spring algal blooms in and beneath sea ice in western Baffin Bay

Oziel L^{1,2*}, P. Massicotte¹, A. Randelhoff¹, J. Ferland¹, A. Vladoiu³, L. Lacour¹, V.
Galindo^{4,6}, S. Lambert-Girard¹, D. Dumont⁴, Y. Cuypers³, P. Bouruet-Aubertot³, C-J Mundy⁶,
J. Ehn⁶, G. Bécu¹, C. Marec^{1,5}, M-H Forget¹, N. Garcia⁷, P. Coupel^{1,7}, P. Raimbault⁷, M-N
Houssais³, M. Babin¹

Affiliations:

¹ Takuvik Joint International Laboratory, Laval University (Canada) - CNRS (France),
Département de biologie et Québec-Océan, Université Laval, Québec, Québec G1V 0A6,
Canada

² Remote Sensing Unit, Bedford Institute of Oceanography, Fisheries and Oceans Canada
P.O. Box 1006, Dartmouth, Nova Scotia, B2Y 4A2, Canada

³ Sorbonne Université (UPMC, Paris6)/CNRS/UPMC/IRD/MNHN, Laboratoire
d'Océanographie et du Climat (LOCEAN), Institut Pierre Simon Laplace (IPSL), 75252 Paris
Cedex 05, France

⁴ Institut des sciences de la mer de Rimouski, Université du Québec à Rimouski, 310 Allée
des Ursulines, Rimouski, Québec G5L 3A1, Canada

⁵ Laboratoire d'Océanographie Physique et Spatiale, UMR 6523, CNRS - IFREMER - IRD -
UBO, Plouzané, France

⁶ Centre for Earth Observation Science, University of Manitoba, Winnipeg, Manitoba R3T
2N2, Canada

⁷ Aix-Marseille University, Mediterranean Institute of Oceanography (MIO), UMR7294,
CNRS/INSU, UMR235, IRD, Marseille, CEDEX 09, France

*Corresponding author's email address: laurent.oziel@takuvik.ulaval.ca,

38 Abstract

39 Arctic sea ice is experiencing a shorter growth season and an earlier ice melt onset. The
40 significance of spring microalgal blooms taking place prior to sea ice breakup is the subject of
41 ongoing scientific debate. During the Green Edge project, unique time-series data were
42 collected during two field campaigns held in spring 2015 and 2016, which documented for the
43 first time the concomitant temporal evolution of the sea ice algal and phytoplankton blooms in
44 and beneath the landfast sea ice in western Baffin Bay. Sea ice algal and phytoplankton blooms
45 were negatively correlated and respectively reached 26 (6) and 152 (182) mg of chlorophyll *a*
46 per m² in 2015 (2016). Here, we describe and compare the seasonal evolutions of a wide variety
47 of physical forcings, particularly key components of the atmosphere–snow–ice–ocean system,
48 that influenced microalgal growth during both years. Ice algal growth was observed under low-
49 light conditions before the snow melt period and was much higher in 2015 due to less snowfall.
50 By increasing light availability and water column stratification, the snow melt onset marked
51 the initiation of the phytoplankton bloom and, concomitantly, the termination of the ice algal
52 bloom. This study therefore underlines the major role of snow on the seasonal dynamics of
53 microalgae in western Baffin Bay. The under-ice water column was dominated by Arctic
54 Waters. Just before the sea ice broke up, phytoplankton had consumed most of the nutrients in
55 the surface layer. A subsurface chlorophyll maximum appeared and deepened, favored by
56 spring tide-induced mixing, reaching the best compromise between light and nutrient
57 availability. This deepening evidenced the importance of upper ocean tidal dynamics for
58 shaping vertical development of the under-ice phytoplankton bloom, a major biological event
59 along the western coast of Baffin Bay, which reached similar magnitude to the offshore ice-
60 edge bloom.

61 1. Introduction

1
2
3
4
5
6
7
8
9
10
11
12
13
14
15
16
17
18
19
20
21
22
23
24
25
26
27
28
29
30
31
32
33
34
35
36
37
38
39
40
41
42
43
44
45
46
47
48
49
50
51
52
53
54
55
56
57
58
59
60
61
62
63
64
65
66
67
68
69
70
71
72
73
74
75
76
77
78
79
80
81
82
83
84
85
86
87
88
89

During the last four decades, the Arctic Ocean's climate has undergone rapid changes clearly evidenced by the spectacular decline in sea ice extent and thickness, as well as the length of the ice season (Stroeve and Notz, 2018; Serreze and Meier, 2019). Sea ice is an important driver of marine primary production and consequently the whole ecosystem (Post et al., 2013; Meier, 2016). First, the sea ice matrix provides a habitat for microalgae which are incorporated into brine channels during freezing in fall (Arrigo, 2017). Second, sea ice with its snow cover controls the amount of light that penetrates into the underlying water column (e.g., Mundy et al., 2007; Frey et al., 2011; Assmy et al., 2017), and thus the potential photosynthetic activity of microalgae (Leu et al., 2015). Sea ice growth and melt affect the processes responsible for the supply of nutrients to the upper ocean by influencing stratification and mixing (Randelhoff et al., 2017). Recently, the importance of how the changing sea ice affects the under-ice dynamics of microalgae has been recognized in other regions; however, little is known about Baffin Bay (Figure 1).

Low-light conditions are recognized to sustain ice algal growth (Leu et al., 2015; Lacour et al., 2017; Hancke et al., 2018). Although contributions of ice algae to the annual primary production remain highly variable, depending on the season and the region (< 1 to 60%; e.g., Loose et al., 2011; Dupont, 2012; Fernández-Méndez et al., 2015), they are a critical food source for the marine food web especially during the winter (Søreide et al., 2010). The seasonal increase in solar radiation and the subsequent snow and sea ice melt lead to the termination of the ice algal bloom and to an increase in transmitted light and stratification underneath the sea ice (Mundy et al., 2014). This combined effect favors high phytoplankton growth in ice-covered waters as previously documented in the Arctic Ocean (e.g., Fortier et al., 2002; Mundy et al., 2009; Assmy et al., 2017). Under-ice phytoplankton blooms can reach magnitudes similar to or even greater than those observed in the open ocean with carbon fixation rates exceeding 30 g C m⁻² d⁻¹ in one documented instance (Arrigo et al., 2014), and are thought to account for more than half of the net algal community production in the Canadian Archipelago (Matrai and Apollonio, 2013).

90 The Western coast of Baffin Bay in the Canadian Arctic is an Arctic Ocean outflow shelf
91 (Figure 1, Tang et al., 2004; Carmack and Wassmann, 2006). A stable landfast sea ice cover
92 forms along the coast and creates a boundary against the offshore mobile ice pack. The static
93 landfast sea ice has a relatively homogeneous thickness compared to pack ice, favoring the
94 spreading of meltwater on the surface after the onset of snow melt in late spring and the
95 formation of high melt pond coverage (Landy et al., 2015). The presence of melt ponds on the
96 ice surface increases the transmission of light through the sea ice, which can trigger under-ice
97 phytoplankton blooms (Mundy et al., 2009; Ehn et al., 2011; Frey et al., 2011; Arrigo et al.,
98 2012). As part of the Green Edge project, this paper presents a comprehensive and unique time
99 series of physical, chemical and biological parameters collected during two consecutive years,
100 2015 and 2016, in western Baffin Bay. The study objectives are to describe the physical
101 processes at play, from the atmosphere, the snow, and the sea ice to the upper ocean, and to
102 identify their roles in modulating the ice algal and phytoplankton spring bloom. While this
103 paper focuses on the temporal variability beneath the landfast sea ice, an additional paper will
104 investigate the physical processes controlling the bloom in time and space in the Baffin Bay
105 marginal ice zone during the Canadian Coast Guard Ship (CCGS) *Amundsen* cruise in 2016
106 (Randelhoff et al., 2019).

107 108 2. Materials and methods

109
110 The study site was located near the community of Qikiqtarjuaq, south of Qikiqtarjuaq
111 Island, along the eastern coast of Baffin Island (67.48 N, 63.79 W, 350-m water depth), and
112 tightly connected with the Baffin Bay through a 600-m deep trough (Gilbert, 1982) (Figure 1).
113 The sampling was conducted during two consecutive years: from 28 March to 14 July 2015,
114 and from 27 April to 22 July 2016. Sampling ended for the 2015 expedition on 14 July because
115 the melting of sea ice close to the shore created dangerous conditions for snowmobile driving.
116 However, in 2016, the use of an airboat on the fragile sea ice after 11 July allowed the extension
117 of our time series until 22 July 2016.

118 119 2.1 Snow and sea ice data

120
121 Every 2–3 days a sample site was chosen at an undisturbed location randomly selected within
122 a 1.2-km radius throughout the project. At the sample site, 5–8 snow depth measurements were
123 made with a metal ruler. A minimum of four ice cores were collected using an ice corer (2015:
124 Kovacs Mark V 14-cm diameter corer for nutrients and algal biomass, Kovacs Mark IV 9-cm
125 diameter corer for temperature and salinity; 2016: Kovacs Mark IV 9-cm diameter corer). The
126 sea ice thickness and freeboard, i.e., the height of the sea ice surface from the sea surface, were
127 measured through the ice core holes using a thickness gauge (Kovacs Enterprise). Two full ice
128 cores were sampled as described in Miller et al. (2015) to measure vertical profiles of
129 temperature and bulk salinity. Ice temperature was measured at 10-cm intervals using a high-
130 precision thermometer (Testo 720; $\pm 0.1^\circ\text{C}$). For ice salinity, the ice was cut with a handsaw
131 into 10-cm sections, which were stored in plastic containers (Whirl-Pak bags) and later melted
132 at room temperature. Bulk salinity of the melted ice sections was determined using a
133 conductivity probe (2015: WTW 330i handheld conductivity meter; 2016: Thermo Scientific
134 Orion portable salinometer model WP-84TPS) that was calibrated every sampling day with

135 seawater standard (35) and MilliQ water (0). Brine volume fraction (%), a controlling factor
 136 for ice permeability, and brine salinity were calculated for each 10-cm section using the ice
 137 temperature and bulk salinity following Cox and Weeks (1983) and Leppäranta and Manninen
 138 (1988); see Gourdal et al. (2019) for a more detailed description of the method. For the
 139 biological and chemical analyses, at least two bottom 10-cm sections (0–3 cm and 3–10 cm
 140 layers) of ice cores were pooled in a 20-L dark isothermal container, with 10 volumes (ice/water
 141 ratio = 1/10) of filtered seawater (0.22 µm polyvinylidene fluoride filter, PVDF, Thermo Fisher
 142 Scientific) added to minimize osmotic stress on microalgae cells, and melted overnight (Bates
 143 and Cota, 1986; Garrison and Buck, 1986). Analyses (described in Section 2.4) were performed
 144 as soon as the ice had melted, or within 24 h, at room temperature (~ 15 °C). The nutrients
 145 present in the filtered surface seawater were measured separately and corrected for final
 146 estimation of nutrient concentrations in the sea ice sections. In 2016, the filtered seawater was
 147 replaced by artificial seawater (MilliQ water with 35 g of Suprapur® NaCl) which did not
 148 contain nutrients.

149 Continuous measurements of wind speed and air temperature were recorded with a
 150 meteorological station positioned near (< 100 m) the center of the 1.2-km radius (Automated
 151 Meteo Mat equipped with temperature (HC2S3) and wind (05305-L) sensors, Campbell
 152 Scientific). The day of the snow melt onset was identified as the date after which the snow
 153 thickness stopped increasing and when the air temperature approached 0 °C during the day. A
 154 positive air temperature was associated with a strong decrease in the near-infrared (1000 nm)
 155 albedo (measured every sampling day with a custom-built radiometer, Solalb, LGGE), making
 156 it a good indicator for snow melt onset in our case (see Verin et al., 2019, for more details). Sea
 157 ice concentration was inferred from the satellite AMSR2 radiometer dataset on a 3.125-km grid
 158 (Spren et al., 2008). The closest pixel of sea ice concentration was less than 500 m from the
 159 study site. The sea ice breakup was determined as the date when the sea ice concentration was
 160 below 80% and when major cracks appeared around the study site, i.e., when the sea ice at the
 161 study site detached from the landfast ice (Figures S1, S2). Melt ponding onset and ice breakup
 162 were determined visually in the field and cross-checked using: 1) a time-lapse camera installed
 163 on Qikiqtarjuaq Island at 300 m above sea level and aimed south, 2) pictures taken of the study
 164 site from an unmanned aerial vehicle (UAV) almost every sampling day, and 3) satellite data
 165 (‘true color’ images from Landsat-8 and Sentinel-2, Figures S1 and S2).

166 2.2 Optical measurements

167
 168
 169 In-water multispectral radiometric data were acquired every 2–3 days using an underwater
 170 spectroradiometer (IcePRO, Biospherical Instrument Inc.). The IcePRO is a modified version
 171 of the C-OPS made by the same manufacturer (Compact Optical Profiling System; Hooker et
 172 al., 2013) to measure downwelling irradiance ($E_d(z, \lambda)$) and upwelling radiance ($L_u(z, \lambda)$) under
 173 the ice to a depth z of up to 100 m, together with above surface downwelling irradiance
 174 $E_d(0^+, \lambda)$. Photosynthetically available radiation (PAR) at each depth ($PAR(z)$, mol photons m^{-2}
 175 s^{-1}) was calculated as follows:

$$176 \quad PAR(z) = \int_{400}^{700} E_d(\lambda, z) d\lambda$$

180 Daily photosynthetically available radiation ($PAR_{24h}(z)$, mol photons $m^{-2} d^{-1}$) in the water
 181 column was calculated by multiplying surface $PAR_{24h}(0^+)$ by the instantaneous transmittance,
 182 $t(z)$, profile calculated from the C-OPS as follows:

$$PAR_{24h}(z) = PAR_{24h}(0^+) \times t(z)$$

185 where $t(z) = PAR(z) / PAR(0^+)$. In 2015, downwelling shortwave irradiance K ($W m^{-2}$) was
 186 acquired using a pyranometer (CNR4, Kipp and Zonen) between 300 nm and 2800 nm. We
 187 then calculated PAR using the following formula

$$PAR = \frac{fract \times K \times cf \times 10^6}{N_A}$$

189 where $cf = 2.77 \cdot 10^{18}$ photon $s^{-1} W^{-1}$ (Morel and Smith, 1974), N_A is Avogadro's number, and
 190 the factor of 10^6 is used to convert from mol photons to μ mol photons. The PAR fraction, $fract$,
 191 was modulated by a function of the solar zenith angle following Kirk (2011) and references
 192 therein. In 2016, downwelling PAR was directly measured using a LI-190SA instrument (Li-
 193 COR). On regular occasions, instrument failure resulted in missing $PAR_{24h}(0^+)$ measurements
 194 (24 d in 2015 and 5 d in 2016). For these days, $PAR_{24h}(0^+)$ was computed every 3 h using the
 195 Santa Barbara DISORT Atmospheric Radiative Transfer model (SBDART, Ricchiazzi et al.,
 196 1998) as described in Bélanger et al. (2013) and Laliberté et al. (2016).

197 Under a spatially heterogeneous surface of sea ice and snow, measuring a
 198 representative attenuation coefficient over a given large area is challenging because the profiles
 199 are characterized by subsurface light maxima occurring between depths of 5 and 10 m. To
 200 reduce the effect of sea ice surface heterogeneity on irradiance measurements (e.g., Ehn et al.,
 201 2011, Frey et al., 2011; Katlein et al., 2015), the vertical attenuation coefficients of PAR,
 202 $K_d(PAR)$, were calculated by fitting a single exponential function on PAR profiles between 10
 203 and 50 m. Then, estimated $K_d(PAR)$ was used to estimate PAR at 1.3 m ($PAR(1.3m)$), for more
 204 details, see Massicotte et al., 2018). Note that 1.3 m corresponds to the average ice thickness
 205 measured during the field campaign and thus to the first measure under the ice.

206 In the present study, the euphotic zone is defined as the layer between the surface and the
 207 depth where $PAR_{24h}(z) = 0.415$ mol photons $m^{-2} d^{-1}$, denoted $Z_{0.415}$. We prefer to define the
 208 euphotic zone in absolute rather than relative terms (cf. the usual 1% depth) because of large
 209 seasonal variations in incident irradiance at high latitudes, as well as sustained low levels even
 210 during the summer due to sea ice. The threshold adopted here was found to match the 1% depth
 211 in the subtropical North Pacific by Letelier et al. (2004), and was later used by Boss and
 212 Behrenfeld (2010). Lacour et al. (2015) used a lower threshold of 0.1 mol photons $m^{-2} d^{-1}$ for
 213 the North Atlantic. Letelier et al. (2004) measured scalar irradiance using a spherical sensor,
 214 while the C-OPS used in this study measures planar irradiance. Field measurements at the study
 215 site (Matthes et al., 2019) indicate that the conversion from planar to scalar irradiance relies on
 216 a multiplying factor of ~ 1.4 within the upper 20 m of the water column. With the companion
 217 paper (Randelhoff et al., 2019), we estimated that by using planar irradiance, the isolume depths
 218 are underestimated by approximately 1–7 m. The isolume depths in this study are thus
 219 conservative and indicate the depth range at which microalgal growth is greatly favored, but
 220 they are not based on a physiological response.

221 2.3 Hydrographical data and methods

226 Conductivity, temperature and depth (CTD) profiles were collected using a Sea-Bird
 227 Electronics 19plus V2 CTD system (factory calibrated prior to the expedition) deployed from
 228 a 1-m² hole in the ice under a tent (Polarhaven, Weatherhaven) from the surface water down to
 229 350 m. The data were post-processed according to the standard procedures recommended by
 230 the manufacturer and averaged into 1-m vertical bins. Ocean current profiles in the water
 231 column were measured using a downward looking 300 kHz Sentinel Workhorse Acoustic
 232 Doppler Current Profiler (ADCP) by RDI Teledyne mounted just beneath the sea ice bottom
 233 through a 25-cm auger hole. The first valid bin was located at a depth of about 4 m; subsequent
 234 bins were spaced with a 2-m vertical resolution and data were collected every 30 min. Flagged
 235 data due to large tilt angles as well as data associated with estimated errors (percentage of the
 236 signal variance) above 50% were rejected, which led us to consider only the data from depths
 237 between 7 and 40 m. Data were also corrected for the magnetic declination. Mean current
 238 velocities ($\sqrt{\bar{u}^2 + \bar{v}^2}$) were obtained by daily averaging.

239 To identify the origins of the water masses in 2015 and 2016, we derived the “Arctic N-P
 240 relationship” (ANP; Jones et al., 1998; Newton et al., 2013), which basically distinguishes
 241 between waters with Atlantic (ANP = 0) and Pacific (ANP = 1) signatures based on the [NO₃]
 242 vs [PO₄] relationship (Figure S3). More details on this method are described in Newton et al.
 243 (2013) and Randelhoff et al. (2019).

244 We derived a winter mixed layer depth (MLD; Rudels et al., 1996) “baseline” for the study
 245 (Figure S4) based on late April measurements. MLD is the bottom of the density mixed layer,
 246 which is defined as the shallowest depth at which the density exceeds a critical density
 247 difference ($\Delta\sigma = 0.1 \text{ kg m}^{-3}$; see Peralta-Ferriz and Woodgate, 2015), relative to the surface
 248 density. Such a conventional MLD algorithm is less useful later in the year due to strong surface
 249 stratification. Most profiles included in our study do not have such a surface mixed layer.
 250 Therefore, we also calculated an equivalent mixed layer depth h_{BD} or depth of the “buoyancy
 251 deficit” as described in Randelhoff et al. (2017), which is more adapted for describing a
 252 seasonal freshening and continuous vertical density structure. The h_{BD} shoals when the seasonal
 253 stratification increases, and it defines the area where mixing is possible. For this study, the h_{BD}
 254 was derived with a density reference at a depth of 50 m (see Randelhoff et al., 2017) based on
 255 the MLD found in late April.

256 Vertical profiles of water column turbulence were measured on 23 June 2016 during a 13-
 257 h period. We used a self-contained autonomous microprofiler (SCAMP, Precision
 258 Measurement Engineering, California, U.S.A.) falling freely at roughly 0.1 m s^{-1} down to a
 259 maximum depth of 100 m. The dissipation rate of turbulent kinetic energy (ϵ) was obtained
 260 from fitting the theoretical Batchelor spectrum to the SCAMP inferred microstructure
 261 temperature gradient spectrum using the modified maximum likelihood method from Ruddick
 262 et al. (2000) over 1-m deep segments. More details about the method can be found in Cuypers
 263 et al. (2012). The diapycnal diffusivity (K_z) was parameterized as a function of turbulence
 264 intensity (buoyancy Reynolds number Re_b) for different turbulence regimes (Bouffard and
 265 Boegman, 2013). As opposed to the Osborn (1980) formulation, which uses a constant mixing
 266 efficiency that overestimates K_z at high Re_b , this parameterization accounts for the variability
 267 in the mixing efficiency depending on the intensity of the turbulence.

269 *2.4 Nutrients and chlorophyll a*

270
 271 To measure inorganic nutrients, nitrate (NO₃⁻), nitrite (NO₂⁻), phosphate (PO₄³⁻) and
 272 silicate (Si(OH)₄), seawater and melted sea ice samples were filtered through GF/F filters and

273 poured into 20-mL sterile polyethylene flasks. Thereafter, the samples were poisoned with 100
274 μL of mercuric chloride (600 mg per 100 ml) and stored in the dark until analyses in the
275 laboratory using an automated colorimetric procedure (Aminot and Kerouel, 2007). A nitracline
276 depth was defined as the shallowest depth where NO_3^- concentration exceeded $1 \mu\text{M}$, based on
277 depth-interpolated profiles of NO_3^- concentrations.

278 Every second day, seawater samples were collected through the 1-m² hole under the tent at
279 eight depths (among the ice-water interface, 1.5, 5, 10, 20, 40, 60, and 75 m) using Niskin
280 bottles. The concentrations of total chlorophyll *a* (TChl*a*, the sum of chlorophyll *a*, divinyl-
281 chlorophyll *a* and chlorophyllide *a*) in seawater (TChl*a*_w) and melted sea ice samples (TChl*a*_{0-3cm})
282 were measured by high performance liquid chromatography (HPLC, Agilent Technologies
283 1200). Particle samples, collected on GF/F filters, were kept frozen at $-80 \text{ }^\circ\text{C}$ until analysis in
284 the laboratory, as per the protocol described by Ras et al. (2008). Fluorescence profiles, a proxy
285 of chlorophyll *a* concentration, were also estimated with a CTD-mounted chlorophyll *a*
286 fluorometer down to 350 m (Wetlabs ECO-FLRT s/n FLRT-3385).

288 3. Results

290 3.1 Weather conditions

291
292 The late autumn/early winter (October to December) of 2014–2015 was slightly warmer than
293 the same period in 2015–2016 (Figure S5A, Qikiqtarjuaq airport). In December 2014, the
294 monthly average air temperature was about $-20 \text{ }^\circ\text{C}$, while it was $-24 \text{ }^\circ\text{C}$ in December 2015, a
295 month of intense sea ice formation. In both years, strong winds were observed in late autumn.
296 For example, a daily averaged wind speed exceeding 15 km h^{-1} persisted over nine consecutive
297 days between 9 and 17 November 2014. The following year, a storm was detected with a rather
298 short duration of 3 days (24–26 December 2015), but stronger intensity with a daily averaged
299 wind speed of 37 km h^{-1} (red vertical lines, Figure S5B).

300 During the winter (from January to March), temperatures were lower in 2015 than in
301 2016, with a monthly mean air temperature minimum of $-36 \text{ }^\circ\text{C}$ in February 2015 compared to
302 $-28 \text{ }^\circ\text{C}$ in February 2016. The winter in 2015 was one of the coldest of the last 35 years for
303 northern Canada (Figure S6). Weather conditions prior to the field campaigns (from the
304 freezing onset in November to April) were also different in terms of total precipitation (in
305 equivalent water) with values 5 times lower in 2014–2015 compared to 2015–2016 (6.3 mm
306 and 34.2 mm, respectively) (Figure S5D).

307 At the end of April, the air temperature was lower in 2015 compared to 2016 ($-15 \text{ }^\circ\text{C}$
308 and $-10 \text{ }^\circ\text{C}$ respectively; Figure 2A); the year 2016 also experienced warm events ($> 0 \text{ }^\circ\text{C}$) in
309 early May. Sea ice thickness was about 1.2 m in both years, but the snow cover was initially
310 thinner in 2015 than in 2016 ($\sim 20 \text{ cm}$ and 40 cm , respectively; Figure 2D). However, more
311 snowfall events occurred in mid-May 2015 compared to the same time period in 2016 (Figure
312 S5D) leading to a thicker snow layer ($\sim 40 \text{ cm}$ and 30 cm , respectively).

313 By the end of May, snow/ice thickness ranged around 15–40 cm/110–135 cm in 2015
314 and 20–50 cm/115–150 cm in 2016 (Figure 2D). Sea ice was much colder and saltier in May
315 2015, with ice temperatures below $-3 \text{ }^\circ\text{C}$ (Figure 3A) and bulk salinity reaching 12 throughout
316 most of the ice thickness (Figure 3B) compared to barely $-1.5 \text{ }^\circ\text{C}$ and 6, respectively, in May
317 2016. In 2015, the sea ice started to warm and freshen slightly after the air temperature first
318 reached $0 \text{ }^\circ\text{C}$, as well as during the rest of the snow melt period (Figures 2A, 3A). In
319 comparison, in 2016, bulk salinity was very low and homogeneous from May to July, and the

320 ice temperature increased as soon as the air temperature hit 0 °C. In May 2015, the brine volume
 321 was about 50% greater than that observed in 2016 (vertical average of 15% and 10%,
 322 respectively; Figure 3C). During both years, the seasonal variation of the depth-averaged brine
 323 volume in the sea ice increased with time (Figure 3C) ranging from about 6 to 35% in 2015 and
 324 from 7 to 25% in 2016. The proportion of brine volume in the bottom 10 cm of the sea ice cores
 325 was twice as high in 2015 as in 2016 ($24.4 \pm 8.5\%$ and $12 \pm 3.1\%$, respectively; significantly
 326 different: *t*-test, *p*-value = 1.9×10^{-9}).

3.2 Light transmission

331 Light transmittance through the snow and sea ice covers differed between the two years
 332 (Figures 2E, S8). At the beginning of May 2015, about twice as much light was transmitted as
 333 at the same time in 2016. Later on, the situation reversed. Under-ice PAR at 1.3 m (*PAR*(1.3m))
 334 decreased by a factor of 3.6 in 2015 (0.12 to about 0.033 mol photons m⁻² d⁻¹), while it
 335 increased by a factor of 3.2 in 2016 (0.05 to about 0.16 mol photons m⁻² d⁻¹). By the end of
 336 May, *PAR*(1.3m) was on average three times higher in 2016 compared to 2015.

337 In 2015, the snow thickness started to decrease and the temperature rose above 0°C
 338 five days later than in 2016 (8 and 3 June, respectively; Figure 2A,D). These dates marked the
 339 snow melt onset (Figure 2D). During the snow melt period (~ 2 weeks), *PAR*(1.3m) increased
 340 significantly by about a factor of 10 in 2015 (from 0.1 to 1 mol photons m⁻² d⁻¹) and by a factor
 341 of 17 in 2016 (from 0.2 to 3.4 mol photons m⁻² d⁻¹). *PAR*(1.3m) started exceeding the 0.415
 342 mol photons m⁻² d⁻¹ threshold one week after the onset of the snow melt in both years (Figure
 343 2E). Once the snow depth was < 10 cm, i.e., in an advanced melting stage, melt ponds started
 344 to form on 22 June 2015 and 15 June 2016 (Figure 2D). The melt ponds appeared concomitantly
 345 with further warming and freshening of the sea ice (Figure 3). During this melt pond period,
 346 *PAR*(1.3m) continued to increase and reached values three times higher (from 1 to 3.4 mol
 347 photons m⁻² d⁻¹ in 2015 and from 3.6 to 10 mol photons m⁻² d⁻¹ in 2016). By mid-July,
 348 *PAR*(1.3m) had increased by about three orders of magnitude from late April.

349 *PAR*(0+) (atmospheric reference above sea ice) decreased by a factor of two (from 62 to
 350 29 mol photons m⁻² d⁻¹) due to increasing cloudiness from 19 to 25 June 2016. The same factor
 351 of two applied to *PAR*(1.3m) underneath the sea ice (3.4 to 1.6 mol photons m⁻² d⁻¹). In 2015,
 352 PAR measurements were not conducted until the ice breakup (22 July 2015), but the 2016 field
 353 study shows that *PAR*(1.3m) reached values (18 mol photons m⁻² d⁻¹), of about the same order
 354 of magnitude as the above surface *PAR*(0+) (~ 55 mol photons m⁻² d⁻¹) just before the breakup
 355 on 18 July 2016. In contrast, *PAR*(20m) decreased by a factor of three in 2015 and seven in
 356 2016 during the melt pond period until the ice breakup.

3.3 Water masses and currents

360 The conservative temperature-absolute salinity diagram (Figure 4) and the ANP relationship
 361 (Figure S3) allowed us to update the estimates found in the literature (i.e., Tang et al., 2004).
 362 We offer these precise definitions of water masses observed at the study site and for the closest
 363 sampled station during the 2016 CCGS *Amundsen* campaign in the same period (see station
 364 403 in Figure 1):

1. **Atlantic Waters (AW).** These waters are more specifically an Atlantic-derived water mass (Figure 4) defined by a conservative temperature $\Theta > 1^\circ\text{C}$ and absolute salinity $S_A > 34$ (g kg^{-1}), because they are colder and fresher than original Atlantic waters. AW were found generally deeper than 300 m, and only partially captured in 2016. Samples at depth at the study site were actually thermocline water, and nutrient sampling did not extend deeply enough to characterize ANP for this water mass. However, offshore measurements made in 2016 from the CCGS *Amundsen* research icebreaker showed ANP ≤ 0.1 (Randelhoff et al., 2019). In the literature, this water mass has also been referred to as West Greenland Intermediate Waters, West Greenland Current Water or Baffin Bay Intermediate Water (Tang et al., 2004; Münchow et al., 2015).
2. **Arctic Waters (ArW).** These waters are defined by $\Theta < -1^\circ\text{C}$ and $S_A < 33.5$ g kg^{-1} (Figure 4). ArW were the main water masses found at the study site. The range of ArW ANP was 0.4–0.6 from April to June 2015, and 0.6–0.8 during the same time period in 2016. The average was 0.51 in 2015, and increased to 0.62 in 2016. These ArW ANP values are higher than those reported offshore from the CCGS *Amundsen* cruise (Randelhoff et al., 2019).
3. **Surface Meltwaters.** These waters form from ice melt in spring. They remain mainly near the surface and increase in temperature due to contact with the atmosphere and radiative heating, which leads to a very wide range of temperature and salinity. However, they are generally fresher and warmer than the ArW.

The surface signature of the ArW in the top 150 m remained very similar to that of Station 403 of the CCGS *Amundsen* station grid (Figure 4), which suggests that the study site is representative of offshore sites in terms of hydrography.

In late April, before summer stratification, the MLD was about 55 and 58 m deep for 2015 and 2016, respectively (Figure S4). The depth of the MLD coincided well with the depth of the winter overturning (i.e., the depth of the minimum temperature; Figure 4) which ranged from ~ 40 m in 2015 to 70 m in 2016. In both years, the melt pond onset coincided with a decrease in surface salinity in the first 5 m (from 32.5 to 28 g kg^{-1} in 2015 and from 32.2 to 30.6 g kg^{-1} in 2016; Figure 5C) and an increase in the surface temperature (from -1.6 to -0.45 $^\circ\text{C}$ in 2015 and from -1.6 to -0.9 $^\circ\text{C}$ in 2016; Figure 5B).

Whereas in winter the water column was stratified only by salinity gradients (Turner angle $< -45^\circ$; Figure S9), the melt pond period was always characterized by a combined effect of temperature and salinity on stratification ($-45^\circ < \text{Turner angle} < 0^\circ$; Figure S9). Increases in meltwater and solar radiation made the surface water both fresher and warmer, which increased surface stratification by a factor of 10 (Brunt-Väisälä frequency $10\text{ m } N^2 \geq 10^{-4} \text{ s}^{-2}$ against values of $\leq 10^{-5} \text{ s}^{-2}$ before the melt pond onset, 1.5–5 m) in early July (Figure 5D). The meltwater accumulation is also illustrated by the shoaling of the h_{BD} from 25–30 m to about 5–20 m (Figure 5D).

This association between sea ice melt and upper ocean stratification seemed to be timed with maximal current speed fields in early July in both years. This timing corresponded to a spring tide cycle (Figure 5A) with maximum current velocities of about 0.25 m s^{-1} in 2015 and 0.45 m s^{-1} in 2016 recorded between 3 and 11 July. This period also corresponded to maximum mean current speed (~ 0.12 m s^{-1} in 2015; ~ 0.2 m s^{-1} in 2016; Figure 6A) concomitant with a local isopycnal deepening. The daily mean kinetic energy ($\text{KE} = 1/2 [u^2 + v^2]$, at 10 m) was 3–5 times higher on average during the spring tides compared to the neap tides ($\sim 55 \text{ cm}^2 \text{ s}^{-2}$ vs $\leq 15 \text{ cm}^2 \text{ s}^{-2}$ in 2015 and $\sim 150 \text{ cm}^2 \text{ s}^{-2}$ vs $\leq 30 \text{ cm}^2 \text{ s}^{-2}$ in 2016).

413 The water-column profiles of temperature, salinity and density were highly modulated
 414 by this spring-neap tidal cycle, resulting in periodic shoaling and deepening of isolines (Figure
 415 5; see Figure S9 for the entire water-column profile). The amplitude of the isopycnal
 416 oscillations reached several tens of meters ($\sim 20\text{--}30$ m) indicating important baroclinic motions.
 417 The semi-diurnal signal was aliased by the daily sampling so that the observed spring tide
 418 amplitude lagged and was always weaker than the real one, but the apparent periodicity is equal
 419 to the spring-neap cycle modulation duration (~ 4 days). We used a harmonic analysis
 420 (Pawlowicz et al., 2002) to derive predicted tides on each valid bin (from 10 to 40 m). As
 421 expected, the tide was found to be the main driver of local currents explaining about 70% of
 422 their variance, and it was dominated by the semi-diurnal component M2 (Figure S10). The
 423 predicted tidal currents correlated significantly with the total observed ones ($r = 0.60$, $p < 10^{-4}$),
 424 but the prediction underestimated the magnitude of the tidal component of the observed
 425 current. The tidal current appears to have about the same direction and magnitude between 10
 426 m and 40 m (Figure S11), and was roughly aligned with the 350-m isobath (Figure 1). The
 427 amplitude of the tidal currents was about half as large in 2015 than in 2016, which is more
 428 likely to happen with baroclinic currents that are very sensitive to stratification. Modelled tidal
 429 currents from a 2-D barotropic model (WEBTIDE v0.7.1; Collins et al. 2011) gave similar
 430 results (spring tide velocity ~ 4 cm s^{-1}) for both 2015 and 2016.

431 We also recorded a residual signal (total measured – tidal prediction – mean current)
 432 with a 12.5-h period. This signal may be typical of internal waves, especially when measured
 433 on the shelf break of a narrow fjord, where a tidal signal may be modulated on a M2 period
 434 (Morozov and Paka, 2010) and result in an isopycnal oscillation such as the one observed at
 435 the study site. The rest of the signal can be attributed to a weak mean current (Figure 6).
 436 Averaged over the whole time series, the intensity of the mean current peaked at 0.06 m s^{-1} in
 437 2015 and at 0.1 m s^{-1} in 2016 with respective averages of about 0.03 m s^{-1} and 0.045 m s^{-1} . In
 438 2015, the velocity field pointed East in 2015 from late April until mid-May. It then shifted
 439 North, and finally, after mid-June, it pointed West (in-fjord). In 2016, the velocity field was
 440 much more stable, almost constantly facing West.

442 *3.4 Mixing and turbulence over one M2 tidal cycle (13 h)*

444 The median profile of the rate of dissipation of turbulent kinetic energy (ϵ) over the entire 13-
 445 h deployment period shows a 20-25 m thick top layer of elevated dissipation rate with values
 446 above 10^{-8} W kg^{-1} (Figure 7). Deeper, in the more stratified layer, an alternation of low and
 447 high ϵ was observed, suggesting internal wave-breaking events.

448 An overview of the ϵ profiles over the 13-h high-frequency sampling period reveals
 449 that higher dissipation occurred during the first half of the sampling period when currents were
 450 stronger (Figure 8). As the tides dominate the current and the SCAMP sampling was taken at
 451 spring tide, spanning a complete tidal cycle, we assume that the mean dissipation rate in Figure
 452 7 is representative of an upper bound for the 2016 period during an early stratification stage.
 453 Dissipation was likely lower in 2015 due to weaker currents.

454 The mean (time-averaged over the 13-h period) mixing coefficient K_z , also called
 455 turbulent or eddy diffusivity, indicates the capability of the flow to mix tracers like heat, salt,
 456 nutrients, or algae. K_z reveals a complex vertical structure. A very thin ice meltwater layer had
 457 started to form a few days prior to the SCAMP deployment, and it drove a marked reduction in
 458 K_z in the first few meters because strong stratification inhibits vertical mixing. Nonetheless, K_z
 459 was more elevated in the mixing layer (3.4×10^{-4} m² s^{-1}) and weaker below (2.1×10^{-4} m² s^{-1}).
 460 Therefore, a parcel located in the mixing layer could be vertically mixed and transported over

461 a length scale of about 1.2 m every day, simply based on the dimensional argument that
 462 diffusivity is a length scale squared divided by a timescale ($K_z = H^2 / dt$). This number falls to
 463 0.7 m d⁻¹ below the mixing layer.

464 Note that the values measured by the SCAMP below the thin meltwater layer are
 465 representative of well-mixed conditions in the upper 20 m (see Fig 5D). Following the SCAMP
 466 deployment, the upper 20 m progressively re-stratified and we expect K_z to decrease there.

468 3.5 Inorganic nutrients and algal biomass

469
 470 The bulk concentration of nitrate + nitrite in the bottom 10-cm segments of the sea ice, $[\text{NO}_3^-$
 471 $+\text{NO}_2^-]_{0-10\text{cm}}$, differed between the two years (Figure 9B). In 2015, $[\text{NO}_3^-+\text{NO}_2^-]_{0-10\text{cm}}$ increased
 472 from 1–9 $\mu\text{mol L}^{-1}$ to almost 30 $\mu\text{mol L}^{-1}$, then collapsed to $\sim 0 \mu\text{mol L}^{-1}$ three days after snow
 473 melt onset (8 June). In 2016, $[\text{NO}_3^-+\text{NO}_2^-]_{0-10\text{cm}}$ was much lower, starting at 3–5 $\mu\text{mol L}^{-1}$ in
 474 early May, then continuously decreasing until depletion on 27 June. Integrated biomass in the
 475 bottom 0–3 cm of the sea ice, $\text{TChl}a_{0-3\text{cm}}$, slightly increased until reaching a maximum just
 476 before the snow melt onset (26 mg m⁻² on 27 May 2015; 6 mg m⁻² on 30 May 2016; Figure
 477 9C). After the snow melt onset, $\text{TChl}a_{0-3\text{cm}}$ decreased to values less than 10 mg m⁻² in 2015 and
 478 less than 2 mg m⁻² in 2016. Overall, the averaged sea ice algal biomass was about four times
 479 lower in 2016 ($1.95 \pm 1.45 \text{ mg m}^{-2}$) than in 2015 ($8.33 \pm 5.88 \text{ mg m}^{-2}$).

480 Following the same pattern as that of $\text{TChl}a_{0-3\text{cm}}$, nitrate+nitrite concentration $[\text{NO}_3^-+\text{NO}_2^-$
 481 $]$ in the surface layer of the water column (see $[\text{PO}_4^{3-}]$ and $[\text{Si}(\text{OH})_4]$ in Figure S12) increased
 482 slightly until reaching a maximum just before snow melt onset (5.4 $\mu\text{mol L}^{-1}$ in 2015 and 5.2
 483 $\mu\text{mol L}^{-1}$ in 2016 at 1.5 m; Figure 9D). The water-column integrated biomass $\text{TChl}a_w$ (Figure
 484 9C) was negatively correlated with ice algal $\text{TChl}a_{0-3\text{cm}}$ ($r = -0.54$, $p = 10^{-3}$ in 2015; $r = -0.60$,
 485 $p = 8 \cdot 10^{-4}$ in 2016) and with $[\text{NO}_3^-+\text{NO}_2^-]$ ($r = -0.91$ in 2015; $r = -0.84$ in 2016, at 5 m, $p <$
 486 10^{-4}). For example, $\text{TChl}a_w$ decreased locally between 27 May and 3 June 2015 while $\text{TChl}a_{0-3\text{cm}}$
 487 $\text{TChl}a_{0-3\text{cm}}$ increased. In contrast, $\text{TChl}a_w$ increased as soon as $\text{TChl}a_{0-3\text{cm}}$ decreased in early June in
 488 both years. After melt pond onset, $\text{TChl}a_w$ rapidly increased to reach a similar maximum in
 489 both years: about 152 mg m⁻² on 12 July 2015 and 182 mg m⁻² on the same date in 2016.
 490 Nutrients also decreased faster, and were almost completely depleted by 10 July 2016 in the
 491 surface layer. While nutrients were also depleted at depth in 2016, $[\text{NO}_3^-+\text{NO}_2^-]$ remained
 492 almost unchanged at 40 m deep ($\sim 5 \mu\text{mol L}^{-1}$) in 2015. The average under-ice phytoplankton
 493 biomass was similar in both years when derived over the same period ($30.4 \pm 41.4 \text{ mg m}^{-2}$ in
 494 2015 and $37.6 \pm 52.0 \text{ mg m}^{-2}$ in 2016, between 27 April and 14 July).

495 Water column $\text{TChl}a_w$ was depth-integrated down to the deepest measurement, but the
 496 resulting values could be underestimates, as non-negligible $[\text{TChl}a_w]$ could exist at greater
 497 depth where no measurements were available. Using smoothed $[\text{TChl}a_w]$ profiles (a 5-point
 498 running median filter followed by a 7-point running mean filter) measured with the fluorometer,
 499 we were able to quantify this underestimation: it ranged from 5 to 60% in 2015 and from 2 to
 500 50% in 2016 (Figure S13). On average, depth-integrated $\text{TChl}a_w$ was underestimated by 28%
 501 in 2015 and by 18% in 2016. The high underestimate of 60% was found on 2 May 2015, and
 502 50% on the same date in 2016, but these underestimations only affect profiles with very low
 503 $\text{TChl}a_w$ (6 mg m⁻² and 2.5 mg m⁻², respectively).

505 4. Discussion

507 4.1 Ocean dynamics

508 4.1.1 Advection

509

510 The study site was representative of the upper open ocean of western Baffin Bay in
 511 terms of water masses (Tang et al., 2004; Curry et al., 2014; Randelhoff et al., 2019), which are
 512 strongly influenced by ArW flowing southward from the northern passages (from North to
 513 South: Nares, Jones, and Lancaster straits with respective sills about 250, 120 and 125 m deep;
 514 see Figure 1 in Wu et al., 2012) and carrying with them a Pacific-origin signature (Tremblay et
 515 al., 2015). This fresh, cold ArW mass meets and overlies the re-circulating AW from the West
 516 Greenland Current that have been thoroughly modified and altered since their departure from
 517 the North Atlantic. The Pacific influence seems to have been more pronounced in 2016 (higher
 518 ANP values), and may be responsible for the greater subsurface stratification (40 m and below).
 519 The ArW generally carry their strong stratification throughout the winter (i.e., they are rarely
 520 homogenized), as evidenced by strong subsurface stratification long before the onset of the melt
 521 period at depth (100–200 m; Figure S9). The increased subsurface stratification and mean
 522 currents in 2016 appear to be linked through the large-scale circulation in Baffin Bay (Figure
 523 S14).

524 To understand whether the phytoplankton biomass observed at the study site (here
 525 dominated by diatoms; P-L Grondin, personal communication) may have been produced
 526 beyond the ice edge in open waters and then transported to the study site, we can consider the
 527 following simple calculations. A maximum mean velocity of about 0.045 m s^{-1} means that
 528 water from the ice edge, which was located more than 200 km away before July of both years
 529 (Figure S15), would have been in transit for a minimum of 52 d to reach the study site. In early
 530 July, the distance from the ice edge to the study site decreased to less than 100 km decreasing
 531 by a factor of two the minimum travel time needed for a water parcel to move from one place
 532 to the other. Therefore, with a typical diatom sinking rate of 1 m d^{-1} (Riebesell, 1989), a diatom
 533 cell located at the ice edge before July would sink to a depth of $> 52 \text{ m}$ by the time it arrived at
 534 the sampling site. Following the same calculations in early July, a diatom cell would have sunk
 535 by at least 26 m, and therefore out of the mixing layer. However, we suspect the downward
 536 sinking would be much greater because the calculation assumes a spatially uniform, maximum
 537 and linear current extending all the way from the ice edge in the basin into the fjord, a rather
 538 unrealistic condition. At the study site, most phytoplankton biomass was found above 30 m and
 539 is most likely produced locally. In other words, our back-of-the-envelope calculations serve to
 540 show that our measurements at the study site were not subject to a highly advective regime and
 541 that the observed under-ice phytoplankton bloom is produced locally.

542

543 4.1.2 Tides and mixing

544

545 Using a harmonic analysis, we showed that current velocities were dominated largely by tides.
 546 This idea was further corroborated by the tidal modulation of the dissipation of turbulent kinetic
 547 energy and isopycnal depths. A parcel located at the study site was likely to move around a
 548 perimeter of 1 to 2.7 km, oscillating on a M2 tidal cycle period (12.42 h, averaged velocities =
 549 $0.045\text{--}0.12 \text{ m s}^{-1}$). While the stronger mean current in 2016 may have been influenced by a
 550 large-scale circulation intensification, the stronger tides were probably due to a constructive
 551 interference between tidal components and/or variations in the internal wave field (sensitive to
 552 stratification; e.g., Morozov and Paka, 2010). Our data set does not give us the means to solve
 553 this puzzle; we assume resolving it would necessitate large-scale modelling of Baffin Bay
 554 hydrography and currents. In any case, the year 2016 was more energetic with faster mean, tidal
 555 and residual currents velocities. We suggest that the spring-tidal energy, in particular, may have

556 contributed to the deepening of the surface stratified layer by mixing the melt layer with the
 557 underlying ArW to about 25 m in 2016. This layer corresponded to the mixing layer, where
 558 active turbulent mixing occurred as a result of surface processes leading to the injection of
 559 turbulent kinetic energy (Brainerd and Michael, 1995). The more energetic currents in 2016
 560 (faster mean, tidal and residual currents velocities) led to deeper mixing as illustrated by the
 561 deeper meltwater distribution starting in late June 2016 (Figure 5). In contrast, in 2015 the
 562 meltwater layer was shallower and its freshening and warming were more abrupt and intense.
 563 If the stronger sub-surface stratification in 2016 presumably led to reduced vertical mixing
 564 below 40 m, in the ice-ocean boundary itself, the stronger currents must have led to greater
 565 shear at the surface, producing even more vertical mixing.

566 During strong mixing conditions (i.e., spring tidal cycle in the mixing layer, $K_z = 3.4 \cdot 10^{-4}$
 567 $\text{m}^2 \text{s}^{-1}$, H (mixing layer depth) = 20 m), the turbulent mixing timescale would be about 1 d (T_{min}
 568 = $H^2/K_z = 21.3$ h) which is about the same order of magnitude as phytoplankton
 569 photoacclimation (1–2 d; Cullen and Lewis, 1988) and cell division time (> 1.6 d; Lacour et
 570 al., 2017; these estimations are based on algal culture under nutrient-replete conditions and may
 571 be overestimated when compared to field conditions). During lower mixing conditions (i.e.,
 572 neap tidal cycle), turbulent mixing remains on the same timescale but increased by 50% (T_{min}
 573 = 35 h ~ 1.5 d). Therefore, during spring tides, mixing occurs with a time scale equal to or
 574 shorter than photoacclimation and cell division time, and the mixing layer is homogenized.
 575 On the contrary, if the timescale for the response is shorter (which is likely during a neap tidal
 576 cycle), phytoplankton in a mixed layer may exhibit a vertical gradient associated with
 577 adaptation to ambient light intensities.

578 579 *4.2 Sea ice history and brine volumes*

580
 581 Brine volumes were 50% larger in 2015 than in 2016. This difference was due mainly to large
 582 brine volumes at the bottom of the ice in 2015 ($> 20\%$), whereas 2016 vertical profiles were
 583 surprisingly almost homogeneous. Brine volume is basically a function of both sea ice bulk
 584 salinity and temperature (Petrich and Eicken, 2010, 2017), but a clear offset in bulk salinity
 585 was observed between the two years, as illustrated in Figure S16. In 2015, the bottom sea ice
 586 was about two times as saline, which explained the greater brine volume in the bottom part of
 587 the sea ice. Rapid growth results in more salt entrapment (Cox and Weeks, 1983). Therefore,
 588 brine volume (i.e., bulk salinity) differences may find an answer in sea ice thermodynamic
 589 history. Colder winter air temperatures, shorter freezing period, lower autumnal snowfall (less
 590 insulation) and colder sea ice temperatures are factors that all converge toward a possible faster
 591 ice growth rate in 2015 compared to 2016.

592 The thermodynamic growth of sea ice slows down, however, as the ice thickens, which results
 593 in bulk salinity increasing towards the top of the sea ice. The very low and homogeneous brine
 594 volumes observed in 2016 thus exclude the ice growth rate as the only explanation. A thin layer
 595 of dry snow laid over a thick layer of already wet snow (Verin et al., 2019) in 2016 by the time
 596 the camp was set up. The presence of wet snow indicated that episodic melt events had already
 597 occurred. The ice was also warmer (i.e., more permeable) than in 2015. Brine convection over
 598 the depth of the sea ice can yield significant desalination well before summer (Jardon et al.,
 599 2013), but lack of evidence about the sea ice history (i.e., winter sea ice sampling) hinders
 600 robust interpretation of brine volume in this study. Slower ice growth and more extensive brine
 601 drainage due to warmer ice, however, could explain the low bulk salinity observed that year.
 602 Ice algae, in response to a warming (Campbell et al., 2014) and desalination of the ice cover
 603 (Mundy et al., 2005), have been shown to slough from the ice bottom. Thus, an early drainage

604 event could have caused a sloughing event of ice algal biomass prior to the commencement of
 605 our study in 2016, potentially influencing the low biomass accumulation observed in 2016.

606

607 *4.3 The roles of clouds, snow, melt ponds and ice algae on light availability*

608

609 Light availability below landfast sea ice is driven by the properties of 1) the incident light field
 610 that results from celestial mechanics, cloudiness, and cloud optical thickness; 2) sea ice surface
 611 conditions (e.g., snow, melt pond, white or bare ice); and 3) sea ice properties (e.g., thickness,
 612 brine volume, ice algae concentration) (Petrich and Eicken, 2017). Here we briefly discuss the
 613 relative contributions of cloud, snow and ice algae in driving under-ice light availability in 2015
 614 and 2016.

615 The month of May 2015 provided an excellent case study for estimating the relative impacts
 616 of snow and ice algae on light availability. Indeed, we observed a decrease in transmittance at
 617 1.3 m concomitantly with snowfalls (Figure 2D,E) and an increase in TChl_{a0-3cm} (Figure 8). At
 618 the beginning of May 2015, before snow melt onset, sea ice transmittance was about 0.2%. By
 619 mid-May, snowfalls had added > 10 cm to the snowpack, reducing the transmittance to a
 620 minimum of 0.06%. The new snow corresponded to a decrease in transmittance by a factor of
 621 3.3, while TChl_{a0-3cm} remained roughly constant around $6.9 \pm 2.6 \text{ mg m}^{-2}$. Over the season, the
 622 transmittance was significantly negatively correlated with snow thickness ($r = -0.74$, $p < 10^{-4}$
 623 in 2015; $r = -0.78$, $p < 10^{-4}$ in 2016).

624 By the end of May 2015, TChl_{a0-3cm} increased from about 6.9 to 26 mg m^{-2} , while snow
 625 thickness averaged around $35 \pm 5 \text{ cm}$. Based on the relationship between $K_d(\text{PAR})$ and TChl_{a0-3cm}
 626 in Ehn and Mundy (2013), we calculated a transmittance of $T = 0.65 \%$ (6.9 mg m^{-2}) and $T = 0.41 \%$
 627 (26 mg m^{-2}) for the bottom ice algae layer (3 cm). Such an increase in ice algae
 628 biomass in the bottom sea ice layer would thus account for a decrease in transmittance by a
 629 factor of 1.6, half the decrease due to snowfall.

630 During the 2015 (2016) snow melt period, transmittance increased by a factor of 25 (20)
 631 from about 0.18% (0.3%) to more than 4.6% (6%). During the melt pond period, transmittance
 632 increased by a factor of 1.6 (4.3) up to 7.5% (26%). The lower 2015 values are due to sampling
 633 ending before the ice breakup. Melt ponds forming over sea ice increased the light transmittance
 634 in the water column, in agreement with Nicolaus et al. (2012) but at a slower rate compared to
 635 the snow melt period. Additionally, we showed that an increase in cloud cover can decrease
 636 both $\text{PAR}(0+)$ and under-ice $\text{PAR}(1.3\text{m})$ by a factor of two (Section 3.1).

637 In summary, our findings demonstrate that the snow thickness had the most significant
 638 attenuation contribution and largely controlled the spring under-ice light availability, in
 639 agreement with literature (i.e., Mundy et al., 2005; Leu et al., 2015; Hancke et al., 2018).

640

641 *4.4 Bloom dynamics: from environmental conditions to algal biomass*

642

643 Here we discuss the environmental conditions that likely controlled the algal bloom dynamics.
 644 The ice algal and phytoplankton phenology seemed similar for both years and can be divided
 645 into three main phases, but contrasting environmental conditions between 2015 and 2016 might
 646 explain the differences in the bloom magnitude and distribution. An illustration of the main
 647 environmental factors driving the evolution of the phytoplankton bloom is shown in Figure 10.

648

- 649 • **Snow-covered period.** Moderate TChl_{a0-3cm} values around 4–10 mg m^{-2} were
 650 observed in April 2015, when winter conditions still prevailed. This finding agrees with

651 recent results from Hancke et al. (2018) who observed ice algal accumulation in low-
 652 light conditions and thick snow cover (> 15 cm). The ice algal bloom reached a
 653 maximum of 26 mg m^{-2} in 2015 and 6 mg m^{-2} in 2016 in late May. The average ice
 654 algal biomass was about four times higher in 2015, which was likely due to better light
 655 conditions (thinner snow cover until mid-May) in 2015 and, potentially, an early
 656 sloughing event prior to the commencement of observations in 2016. This result
 657 confirms the negative relationship between snow depth and ice algae biomass during
 658 its early development phase found by Campbell et al. (2015). In 2015, bulk ice nutrient
 659 concentrations correlated with ice algal biomass ($\text{TChl}a_{0-3\text{cm}}$; $r_{[\text{NO}_3+\text{NO}_2-]} = 0.8$; $r_{[\text{PO}_4^{3-}]}$
 660 $= 0.74$, $r_{[\text{Si}(\text{OH})_4]} = 0.47$; $p < 10^{-3}$) and showed elevated concentrations in the ice bottom
 661 relative to those in the interface water, suggesting that a nutrient ‘concentration
 662 mechanism’ was at play in sea ice. Similar observations have been made previously
 663 and have been suggested to be associated with a release of intracellular pools due to
 664 osmotic shock during ice melt processing (Cota et al., 1990, 2009; Harrison et al., 1990;
 665 Pineault et al., 2013; Torstensson et al., 2019) or via production of biofilms by sea ice
 666 diatoms and bacteria that potentially trap nutrients (Krembs et al., 2002, 2011; Steele
 667 et al., 2014). Bacterial activity may also have played a role through nutrient
 668 remineralization (Fripiat et al. 2014, 2017; Firth et al., 2016). By reducing the light
 669 transmitted to the upper water column, the snowfall in mid-May constrained
 670 phytoplankton growth to the very surface. For both years, the pre-bloom period was
 671 characterized by a much deeper h_{BD} (~ 30 m) than $Z_{0.415}$ that was located close to the
 672 surface. In those conditions, vertical mixing could potentially export phytoplankton out
 673 of the euphotic layer and disrupt phytoplankton growth (Behrenfeld and Boss, 2018).
 674 In general, we observed low biomass ($\leq 0.5 \text{ mg m}^{-3}$) in both years, with a maximum at
 675 the surface.

- 676
 677 • **Snow melt period.** This period was characterized by a rapid snow melt that led to the
 678 near-disappearance of the snow on the sea ice surface. The progression strongly
 679 increased the amount of light transmitted to the upper water column by more than one
 680 order of magnitude and significantly deepened $Z_{0.415}$ (Figure 10) demonstrating the
 681 major role of snow on light transmission (Mundy et al., 2005; Leu et al., 2015). For
 682 example, in 2016, the greater amount of winter precipitation, warmer air temperatures,
 683 and the earlier melt onset led to a more pronounced and earlier deepening of $Z_{0.415}$. In
 684 line with previous studies in Resolute Passage (Fortier et al., 2002; Galindo et al., 2014;
 685 Mundy et al., 2014), on Green Edge data (Galindo et al., 2017) or at pan-Arctic scale
 686 (Leu et al., 2015), the snow melt onset also coincided with the effective end of the ice
 687 algal bloom, possibly because of a brine flushing as indicated by the decrease in brine
 688 salinity resulting in an ablation of ice algal habitat. The ice algae then sloughed from
 689 the sea ice into the underlying water column. The concurrent increase in phytoplankton
 690 [$\text{TChl}a_w$] in surface water at that specific time may have resulted from this release of
 691 ice algae. The possible seeding of the phytoplankton spring bloom by ice algae (e.g.,
 692 Olsen et al., 2017; van Leeuwe et al., 2018; Selz et al., 2018) is beyond the scope of
 693 the present paper (but see Grondin, 2019). Freshwater from snow and ice melt started
 694 to accumulate at the ocean surface by the end of the period, and was subsequently
 695 warmed by solar radiation. About one week later, phytoplankton biomass started to
 696 accumulate in the upper water column, which was newly stratified as evidenced by the
 697 shoaling of h_{BD} .
 698

699 • **Melt pond period.** Melt ponds started to form from snow meltwater around the
 700 summer solstice. Consequently, this period was characterized by a continuous increase
 701 in transmitted $PAR(1.3m)$ (Figure 2E), and a deep $Z_{0.415}$ which reached a maximum of
 702 about 30 m in mid-June. Some cloudy periods, demonstrated by a local decrease in
 703 $PAR(0+)$ during the second half of June 2016, may have temporarily dampened this
 704 shoaling of $Z_{0.415}$. After June, $Z_{0.415}$ shoaled to 20 m because of the phytoplankton
 705 accumulation that increased seawater light attenuation. The sea ice melting rate
 706 accelerated the freshening of the ocean surface layer. As meltwaters accumulated
 707 increasingly in the surface layer, stratification increased and the h_{BD} shoaled from 20–
 708 30 m to about 10–20 m at about the same depth as $Z_{0.415}$.

709 The surface layer stratified by meltwater seemed to provide sufficient stability
 710 on average for phytoplankton growth and blooming in the euphotic zone, which rapidly
 711 consumed most of the nutrients. Increasing stratification in the euphotic zone could
 712 also prevent the supply of nutrient-rich deeper water (Randelhoff et al., 2016). A
 713 subsurface chlorophyll maximum (SCM) formed at the base of the surface mixed layer,
 714 corresponding to the best compromise between light and nutrient availability
 715 (McLaughlin and Carmack, 2010; Martin et al., 2012). Over time, the SCM
 716 progressively deepened while nutrients were consumed down to 20–40 m, following
 717 the top of the nitracline and the euphotic depth pattern until the ice breakup (Figure
 718 10). Both the SCM and nitracline deepened earlier to a greater depth in 2016 than in
 719 2015, which may be attributed to a larger spring tide-induced vertical mixing (Mundy
 720 et al., 2014) and to an earlier phytoplankton bloom initiation (earlier $Z_{0.415}$ deepening
 721 and stratification). In this context, phytoplankton were able to reach a greater depth and
 722 a larger nutrient reservoir in 2016.

723 For both years, the concomitant increase in stratification (by two orders of
 724 magnitude) and irradiance (by three orders of magnitude) seemed to control the timing
 725 of phytoplankton bloom initiation (i.e., positive biomass accumulation rate, *sensu* Boss
 726 and Behrenfeld, 2010; Figure S17). The phytoplankton bloom seemed to be triggered
 727 earlier in 2016 (Figure S17). The differences between 2015 and 2016 must be
 728 considered carefully, as the sampling periods were different between years. In both
 729 years, the blooms peaked at about the same time and magnitude (152 mg $TChla_w m^{-2}$
 730 on 12 July 2015 and 182 mg $TChla_w m^{-2}$ on 13 July 2016), and showed quasi-similar
 731 biomass when averaged over the same period (~ 30 and 38 mg $TChla_w m^{-2}$,
 732 respectively).

733 The significant phytoplankton blooms largely dominated the ice algal blooms in terms
 734 of maximum integrated biomass, reaching about 6–30 times the magnitude of the ice algal
 735 blooms. This work confirms previous estimations of the moderate contribution of sea ice algae
 736 in seasonally ice-covered water (e.g., Michel et al., 2006; Loose et al., 2011; Mundy et al.,
 737 2014) and contributes to the understanding of under-ice phytoplankton spring blooms as major
 738 and regular events under landfast sea ice in Baffin Bay (Wassmann and Reigstad, 2011; Leu et
 739 al., 2015; Horvat et al., 2017). Previous studies have documented similar magnitudes of ice
 740 algal blooms (~ 5 – 40 mg $Chla m^{-2}$; Mundy et al., 2014; Leu et al., 2015) and phytoplankton
 741 blooms (~ 400 – 500 mg $Chla m^{-2}$; Fortier et al., 2002; Mundy et al., 2014) in the Canadian
 742 Arctic Archipelago. Based on results of the companion article (Randelhoff et al., 2019), the ice-
 743 edge bloom located farther east in the marginal ice zone in 2016 reached ~ 70 mg $TChla_w m^{-2}$,
 744 less than half of the amount measured in this study (182 mg $TChla m^{-2}$), therefore corroborating
 745 previous estimations that under-ice and ice-edge blooms can have comparable magnitudes

746 (Mayot et al., 2018). Also possible is that the large amount of biomass accumulated at the study
 747 site may be attributed to low or mismatched secondary productio

748 5. Summary and Conclusions

749
 750 During the Green Edge expeditions, we documented for the first time the temporal evolution
 751 of environmental factors driving the microalgal bloom in the sea ice-covered western Baffin
 752 Bay subject to rapid seasonal and interannual changes. Sampling a wide range of physical,
 753 chemical and biological parameters during the two contrasting years of 2015 and 2016 offered
 754 a unique opportunity to compare the succession of events that led to the under-ice algal spring
 755 blooms. The contrasting seasonal progression led to the different timing and magnitude of the
 756 blooms.

757 First of all, the atmospheric forcings during the preceding winters pre-conditioned the
 758 sea ice algal bloom differently for each year. The winter of 2014–2015 was colder with less
 759 snowfall than the 2015–2016 winter. As a consequence, twice the amount of light was
 760 transmitted to the bottom ice and the average ice algal biomass in 2015 was more than four
 761 times higher than in 2016. Our findings illustrate the critical need for year-round *in situ*
 762 sampling, especially to get a better understanding of the incorporation of sea ice algae into the
 763 sea ice during its formation and possible early brine drainage at the end of winter, and the
 764 impact of these physical processes on ice algal development.

765 Beneath the sea ice, the water at the study site displayed characteristics that, as
 766 expected, were representative of the hydrological conditions in offshore western Baffin Bay.
 767 The water column was largely influenced by the inflowing ArW modulated by spring-neap tidal
 768 currents. We observed differences between years: in 2016, the water column was more
 769 influenced by Pacific Waters and experienced more than 30% faster current velocities
 770 compared with 2015. The snow melt onset marked the termination of the ice algal bloom (likely
 771 sloughed in the water column) and a concomitant phytoplankton bloom initiation in the surface
 772 of the water column, typically linked to an increase in both stratification and light availability.
 773 Whereas more PAR penetrated the sea ice immediately after the onset of snow melt, biomass
 774 did not accumulate significantly until the onset of haline stratification and hence the reduction
 775 of mixing (i.e., melt pond period). This study underlines the major role of snow in vertical light
 776 attenuation compared to that of the sea ice, melt ponds, or even the ice algae themselves in the
 777 landfast sea ice of western Baffin Bay. Strong stratification due to meltwater accumulation was
 778 found to inhibit the supply of nutrients to the surface water layer, which became depleted in
 779 nutrients about two weeks after the snow melt onset. Spring tides enhanced the mixing of
 780 meltwaters with underlying ArW, resulting in a deeper surface layer reaching 40 m in 2016.
 781 The phytoplankton then developed at sub-surface following the best compromise between light
 782 and nutrient availability. Once the ice broke up at the end of the sampling period in July, the
 783 depth of the sub-surface chlorophyll maximum further deepened in the marginal ice zone, while
 784 meltwaters accumulated in the surface layer (see Randelhoff et al., 2019).

785 The significant phytoplankton blooms largely dominated the ice algal blooms in terms
 786 of maximum integrated biomass. This study also illustrates that under-ice phytoplankton
 787 blooms can reach similar or even greater magnitude than ice-edge blooms in marginal ice zones,
 788 contributing to the understanding of under-ice phytoplankton spring blooms as major and
 789 regular events under landfast sea ice in Baffin Bay. With the ongoing warming climate in the
 790 Arctic, the general trend toward thinner sea ice, longer open-water periods (Stroeve and Notz,
 791 2018) and less snowfall (Bintanja, 2018) would drastically increase the availability of light and
 792 affect microalgal growth beneath the Baffin Bay sea ice cover. We can expect that an earlier

793 onset of ice melt may shorten the sea ice algal growth season yet increase the potential for
794 under-ice phytoplankton blooms in Baffin Bay.

1
2
3
4
5
6
7
8
9
10
11
12
13
14
15
16
17
18
19
20
21
22
23
24
25
26
27
28
29
30
31
32
33
34
35
36
37
38
39
40
41
42
43
44
45
46
47
48
49
50
51
52
53
54
55
56
57
58
59
60
61
62
63
64
65

795

796 **References**

797

798 Aminot A, K erouel R. 2007. Dosage automatique des nutriments dans les eaux marines :
799 m ethodes en flux continu. Ed. Ifremer, M ethodes d'analyse en milieu marin, 188 pp.

800

801 Arrigo KR, Perovich DK, Pickart RS, Brown ZW, van Dijken GL et al. 2012. Massive
802 phytoplankton blooms under Arctic sea ice. *Science* 336: 6087.

803 <https://doi.org/10.1126/science.1215065>

804

805 Arrigo KR, Perovich DK, Pickart RS, Brown ZW, van Dijken GL, et al. 2014. Phytoplankton
806 blooms beneath the sea ice in the Chukchi Sea. *Deep Sea Res Pt II* 105: 1–16. ISSN 0967-
807 0645. doi: <http://dx.doi.org/10.1016/j.dsr2.2014.03.018>.

808

809 Assmy P, Fernandez-Mendez M, Duarte P, Meyer A, Randelhoff A, et al. 2017. Leads in
810 Arctic pack ice enable early phytoplankton blooms below snow-covered sea ice. *Sci Rep-UK*
811 7: 40850. <https://doi.org/10.1038/srep40850>

812

813 Bates SS, Cota FC. 1986. Fluorescence induction and photosynthetic responses of Arctic ice
814 algae to sample treatment and salinity. *J Phycol* 70: 421–429. [https://doi.org/10.1111/j.1529-
815 8817.1986.tb02484.x](https://doi.org/10.1111/j.1529-8817.1986.tb02484.x)

816

817 Behrenfeld MJ, Boss, ES. 2018. Student's tutorial on bloom hypotheses in the context of
818 phytoplankton annual cycles. *Glob Change Biol* 24(1): 55–77. DOI:
819 <https://doi.org/10.1111/gcb.13858>

820

821 B elanger S, Babin M, Tremblay J- . 2013. Increasing cloudiness in Arctic damps the increase
822 in phytoplankton primary production due to sea ice receding. *Biogeosciences* 10(6): 4087–
823 4101. <https://doi.org/10.5194/bg-10-4087-2013>

824

825 Bintanja R, Katsman CA, Selten FM. 2018. Increased Arctic precipitation slows down sea ice
826 melt and surface warming. *Oceanography* 31(2): 118–125.
827 <https://doi.org/10.5670/oceanog.2018.204>

828

829 Boss E, Behrenfeld M. 2010. In situ evaluation of the initiation of the North Atlantic
830 phytoplankton bloom. *Geophys Res Lett* 37(18): n/a–n/a. ISSN 00948276. 742.
831 <https://doi.org/10.1029/2010GL044174>

832

- 833 Bouffard D, Boegman L. 2013. A diapycnal diffusivity model for stratified environmental
834 flows. *Dynamics of Atmospheres and Oceans* 61–62: 14–34. Available at:
835 <http://dx.doi.org/10.1016/j.dynatmoce.2013.02.002>
- 836
- 837 Brainerd KE, Michael CG. 1995. Surface mixed and mixing layer depths. *Deep Sea Res Pt I*
838 42(9): 1521–1543. ISSN 0967-0637, [https://doi.org/10.1016/0967-0637\(95\)00068-H](https://doi.org/10.1016/0967-0637(95)00068-H)
- 839
- 840 Campbell KL, Mundy CJ, Barber DG, Gosselin, M. 2014. Remote estimates of ice algae
841 biomass and their response to environmental conditions during spring melt. *Arctic* 67(3): 375–
842 387. <http://dx.doi.org/10.14430/arctic4409>
- 843
- 844 Campbell K, Mundy CJ, Barber DG, Gosselin M. 2015. Characterizing the sea ice algae
845 chlorophyll *a*–snow depth relationship over Arctic spring melt using transmitted irradiance. *J*
846 *Mar Syst* 147: 76–84. <https://doi.org/10.1016/j.jmarsys.2014.01.008>
- 847
- 848 Carmack E, Wassmann P. 2006. Food webs and physical–biological coupling on pan-Arctic
849 shelves: unifying concepts and comprehensive perspectives. *Prog Oceanogr* 71: 446–477.
850 <https://doi.org/10.1016/j.pocean.2006.10.004>
- 851
- 852 Collins AK, Hannah CG, Greenberg D. 2011. Validation of a high-resolution modelling system
853 for tides in the Canadian Arctic Archipelago. *Can Tech Rep Hydrogr Ocean Sci* 273: vii +
854 72pp.
- 855
- 856 Cota GF, Anning, JL, Harris LR, Harrison WG, Smith REH. 2009. Impact of ice algae on
857 inorganic nutrients in seawater and sea ice in Barrow Strait, NWT, Canada, during spring. *Can*
858 *J Fish Aquat Sci* 47(7): 1402–1415. <https://doi.org/10.1139/f90-159>
- 859
- 860 Cox GFN, Weeks WF. 1983. Equations for determining the gas and brine volumes in sea-ice
861 samples. *J Glaciol* 29(102): 306–316. <https://doi.org/10.3189/S0022143000008364>
- 862
- 863 Cullen JJ, Lewis M R. 1988. The kinetics of algal photoadaptation in the context of vertical
864 mixing. *J Plankton Res* 10: 1039–1063. <https://doi.org/10.1093/plankt/10.5.1039>
- 865
- 866 Curry B, Lee CM, Petrie B, Moritz RE, Kwok R. 2014. Multiyear volume, liquid freshwater,
867 and sea ice transports through Davis Strait, 2004–10. *J Phys Oceanogr* 44(4): 1244–1266.
868 <https://doi.org/10.1175/JPO-D-13-0177.1>
- 869
- 870 Cuypers Y, Bouruet-Aubertot P, Marec C, Fuda JL. 2012. Characterization of turbulence from
871 a fine-scale parameterization and microstructure measurements in the Mediterranean Sea

872 during the BOUM experiment. *Biogeosciences* 9(8): 3131–3149. ISSN 1726-4189.
873 <https://doi.org/10.5194/bg-9-3131-2012>

874

875 Dupont F. 2012. Impact of sea-ice biology on overall primary production in a biophysical
876 model of the pan-Arctic Ocean. *J Geophys Res* 117: C00D17.
877 <https://doi.org/10.1029/2011JC006983>

878

879 Ehn, JK, Mundy CJ, Barber DG, Hop H, Rossnagel A, Stewart J. 2011. Impact of horizontal
880 spreading on light propagation in melt pond covered seasonal sea ice in the Canadian Arctic. *J*
881 *Geophys Res* 116: C00G02. <https://doi.org/10.1029/2010JC006908>

882

883 Ehn JK, Mundy CJ. 2013. Assessment of light absorption within highly scattering bottom sea
884 ice from under-ice light measurements: implications for Arctic ice algae primary production.
885 *Limnol Oceanogr* 58: 893–902. <https://doi.org/10.4319/lo.2013.58.3.0893>

886

887 Fernández-Méndez M, Katlein C, Rabe B, Nicolaus M, Peeken I, Bakker K, et al. 2015.
888 Photosynthetic production in the Central Arctic during the record sea-ice minimum in 2012.
889 *Biogeosciences* 12: 2897–2945. <https://doi.org/10.5194/bgd-12-2897-2015>

890

891 Firth E, Carpenter SD, Sørensen HL, Collins RE, Deming JW. 2016. Bacterial use of choline
892 to tolerate salinity shifts in sea-ice brines. *Elem Sci Anth* 4: 000120.
893 <https://doi.org/doi:10.12952/journal.elementa.000120>

894

895 Fortier M, Fortier L, Michel C, Legendre L. 2002. Climatic and biological forcing of the vertical
896 flux of biogenic particles under seasonal Arctic sea ice. *Mar Ecol Progr Ser* 225(1): 1–16.
897 <https://doi.org/10.3354/meps225001>

898

899 Frey KE, Perovich DK, Light B. 2011. The spatial distribution of solar radiation under a melting
900 Arctic sea ice cover. *Geophys Res Lett* 38(22): 1–6. <https://doi.org/10.1029/2011GL049421>

901

902 Fripiat F, Sigman DM, Fawcett SE, Rafter PA, Weigand MA, Tison JL. 2014. New insights
903 into sea ice nitrogen biogeochemical dynamics from the nitrogen isotopes. *Global Biogeochem*
904 *Cy* 28(2): 115–130. <https://doi.org/doi:10.1002/2013gb004729>

905

906 Fripiat F, Meiners KM, Vancoppenolle M, Papadimitriou S, Thomas DN, Ackley SF, . . . Tison
907 JL. 2017. Macro-nutrient concentrations in Antarctic pack ice: Overall patterns and overlooked
908 processes. *Elem Sci Anth* 5: 13. <https://doi.org/doi:10.1525/elementa.217>

909

- 910 Galindo V, Gosselin M, Lavaud J, Mundy CJ, Else B, Ehn J, Babin B, Rysgaard S. 2017.
911 Pigment composition and photoprotection of Arctic sea ice algae during spring. *Mar Ecol*
912 *Progr Ser* 585: 49–69. <https://doi.org/10.3354/meps12398>
913
- 914 Galindo V, Levasseur M, Mundy CJ, Gosselin M, Tremblay JÉ, Scarratt M, Gratton Y,
915 Papakiriakou T, Poulin M, Lizotte M. 2014. Biological and physical processes influencing sea
916 ice, under-ice algae, and dimethyl-sulfoniopropionate during spring in the Canadian Arctic
917 Archipelago. *J Geophys Res* 119: 3746–3766, <https://doi.org/10.1002/2013JC009497>
918
- 919 Garrison DL, Buck KR. 1986. Organism losses during ice melting: a serious bias in sea ice
920 community studies. *Polar Biol* 6: 237–239, <https://doi.org/10.1007/BF00443401>
921
- 922 Gilbert R. 1982. Contemporary sedimentary environments on Baffin Island, N.W.T., Canada:
923 glaciomarine processes in fiords of eastern Cumberland Peninsula. *Arctic Alpine Res* 14: 1–
924 12. <https://www.jstor.org/stable/1550809>
925
- 926 Gourdal M, Crabeck O, Lizotte M, Galindo V, Babin M, Scarratt M, Gosselin M, Scarratt M,
927 Levasseur M. 2019. Upward transport of bottom ice dimethyl sulfide during the advanced
928 melting stage of arctic first-year sea ice. *Elem Sci Anth* (accepted).
929
- 930 Grondin PL. 2019. Algal taxonomic succession and its drivers during under-ice spring blooms
931 in Baffin Bay. Msc thesis, Laval University.
932
- 933 Hancke K, Lund-Hansen LC, Lamare ML, Højlund Pedersen S, King MD, Andersen P, Sorrell
934 BK. 2018. Extreme low light requirement for algae growth underneath sea ice: A case study
935 from Station Nord, NE Greenland. *J Geophys Res-Oceans* 123: 985–1000.
936 <https://doi.org/10.1002/2017JC013263>
937
- 938 Harrison WG, Cota GF, Smith REH. 1990. Nitrogen utilization in ice algal communities of
939 Barrow Strait, Northwest Territories, Canada. *Mar Ecol Progr Ser* 67(3): 275–283.
940
- 941 Hooker SB, Morrow JH, Matsuoka, A. 2013. Apparent optical properties of the Canadian
942 Beaufort Sea – Part 2: The 1% and 1 cm perspective in deriving and validating AOP data
943 products. *Biogeosciences* 10: 4511–4527. <https://doi.org/10.5194/bg-10-4511-2013>
944
- 945 Horvat C, Jones DR, Iams S, Schroeder D, Flocco D, Feltham D. 2017. The frequency and
946 extent of sub-ice phytoplankton blooms in the Arctic Ocean. *Sci Adv* 3:e1601191.
947 <https://doi.org/10.1126/sciadv.1601191>
948

- 949 Jardon FP, F Vivier, M Vancoppenolle, A Lourenço, P Bouruet-Aubertot, Y Cuypers. 2013.
950 Full-depth desalination of warm sea ice. *J Geophys Res-Oceans* 118(1): 435–447.
951 <https://doi.org/10.1029/2012JC007962>
952
- 953 Juhl AR, Krembs C. 2010. Effects of snow removal and algal photoacclimation on growth and
954 export of ice algae. *Polar Biol* 33: 1057–1065. <https://doi.org/10.1007/s00300-010-0784-1>
955
- 956 Katlein C, Arndt S, Nicolaus M, Perovich DK, Jakuba MV, et al. 2015. Influence of ice
957 thickness and surface properties on light transmission through Arctic sea ice. *J Geophys Res-*
958 *Oceans* 120(9): 5932–5944. ISSN 21699275. <https://doi.org/10.1002/2015JC010914>
959
- 960 Kirk JTO. 2011. *Light and Photosynthesis in Aquatic Ecosystems*, 3rd edn. Cambridge:
961 Cambridge University Press, p 151. <https://doi.org/10.1017/CBO9781139168212>
962
- 963 Krembs C, Eicken H, Junge K, Deming JW. 2002. High concentrations of exopolymeric
964 substances in Arctic winter sea ice: implications for the polar ocean carbon cycle and
965 cryoprotection of diatoms. *Deep-Sea Res Pt I* 49(12): 2163–2181. ISSN 0967-0637,
966 [https://doi.org/10.1016/S0967-0637\(02\)00122-X](https://doi.org/10.1016/S0967-0637(02)00122-X)
967
- 968 Krembs C, Eicken H, Deming JW. 2011. Exopolymer alteration of physical properties of sea
969 ice and implications for ice habitability and biogeochemistry in a warmer Arctic. *Proc Natl*
970 *Acad Sci USA* 108(9): 3653–3658. <https://doi.org/10.1073/pnas.1100701108>
971
- 972 Kwok R. 2018. Arctic sea ice thickness, volume, and multiyear ice coverage: losses and coupled
973 variability (1958–2018). *Environ Res Lett* 13: 105005. [https://doi.org/10.1088/1748-](https://doi.org/10.1088/1748-9326/aae3ec)
974 [9326/aae3ec](https://doi.org/10.1088/1748-9326/aae3ec)
975
- 976 Lacour L, Claustre H, Prieur L, D'Ortenzio F. 2015. Phytoplankton biomass cycles in the North
977 Atlantic subpolar gyre: a similar mechanism for two different blooms in the Labrador Sea.
978 *Geophys Res Lett* 42: 5403–5410. <https://doi.org/10.1002/2015GL064540>
979
- 980 Lacour T, Larivière J, Babin M. 2017. Growth, Chl *a* content, photosynthesis, and elemental
981 composition in polar and temperate microalgae. *Limnol Oceanogr* 62: 43–58.
982 <https://doi.org/10.1002/lno.10369>
983
- 984 Laliberté J, Bélanger S, Frouin R. 2016. Evaluation of satellite-based algorithms to estimate
985 photosynthetically available radiation (PAR) reaching the ocean surface at high northern
986 latitudes. *Remote Sens Environ* 184: 199–211. <https://doi.org/10.1016/j.rse.2016.06.014>
987

- 988 Landy JC, Ehn JK, Barber DG. 2015. Albedo feedback enhanced by smoother Arctic sea ice.
989 *Geophys Res Lett* 42(24): 10,714–10,720. <https://doi.org/10.1002/2015GL066712>
- 990
- 991 Letelier RM, Karl DM, Abbott MR, Bidigare RR. 2004. Light driven seasonal patterns of
992 chlorophyll and nitrate in the lower euphotic zone of the North Pacific Subtropical Gyre.
993 *Limnol Oceanogr* 49(2): 508–519. ISSN 00243590. <https://doi.org/10.4319/lo.2004.49.2.0508>
- 994
- 995 Leppäranta M, Manninen T. 1988. The brine and gas content of sea ice with attention to low
996 salinities and high temperatures. Internal Rep 88-2, Finn Inst Mar Res, Helsinki.
- 997
- 998 Leu E, Mundy C, Assmy P, Campbell K, Gabrielsen T, et al. 2015. Arctic spring awakening:
999 Steering principles behind the phenology of vernal ice algal blooms. *Progr Oceanog* 139: 151–
1000 170. ISSN 0079-6611. <https://doi.org/10.1016/j.pocean.2015.07.012>
- 1001
- 1002 Loose B, Miller LA, Elliott S, Papakyriakou T. 2011. Sea ice biogeochemistry and material
1003 transport across the frozen interface. *Oceanography* 24(3): 202–218.
1004 <http://dx.doi.org/10.5670/oceanog.2011.72>.
- 1005
- 1006 Lowry K, Van Dijken GL, Arrigo KR. 2014. Evidence of under-ice phytoplankton blooms in
1007 the Chukchi Sea from 1998 to 2012. *Deep-Sea Res Pt II* 105: 105–117.
1008 <http://dx.doi.org/10.1016/j.dsr2.2014.03.013>
- 1009
- 1010 Martin J, Tremblay J-É, Price NM. 2012. Nutritive and photosynthetic ecology of subsurface
1011 chlorophyll maxima in Canadian Arctic waters. *Biogeosciences* 9: 5353–5371.
1012 <http://dx.doi.org/10.5194/bg-9-5353-2012>
- 1013
- 1014 Massicotte P, Bécu G, Lambert-Girard S, Leymarie E, Babin M. 2018. Estimating underwater
1015 light regime under spatially heterogeneous sea ice in the Arctic. *Appl Sci* 8(12): 2693.
1016 <https://doi.org/10.3390/app8122693>
- 1017
- 1018 Matrai, P, Apollonio, S. 2013. New estimates of microalgae production based upon nitrate
1019 reductions under sea ice in Canadian shelf seas and the Canada Basin of the Arctic Ocean.
1020 *Mar Biol* 160(6): 1297–1309.
- 1021
- 1022 Matthes LC, Ehn JK, Girard SL, Pogorzelec NM, Babin M, Mundy CJ. 2019. Average cosine
1023 coefficient and spectral distribution of the light field under sea ice: Implications for primary
1024 production. *Elem Sci Anth* 7: 25. DOI: <https://doi.org/10.1525/elementa.363>
- 1025

- 1026 Mayot N, Matrai P, Ellingsen IH, Steele M, Johnson K, Riser SC, Swift D. 2018. Assessing
1027 phytoplankton activities in the seasonal ice zone of the Greenland Sea over an annual cycle. *J*
1028 *Geophys Res-Oceans* 123: 8004–8025. <https://doi.org/10.1029/2018JC014271>
1029
- 1030 McLaughlin FA, Carmack EC. 2010. Deepening of the nutricline and chlorophyll maximum in
1031 the Canada Basin interior, 2003–2009. *Geophys Res Lett* 37: L24602.
1032 <https://doi.org/10.1029/2010GL045459>
1033
- 1034 Meier WN. 2016. Losing Arctic sea ice: Observations of the recent decline and the long-term
1035 context. In Thomas DN ed, *Sea Ice*, 3rd Edition. John Wiley & Sons, Ltd, pp 290–303.
1036 <https://doi.org/10.1002/9781118778371.ch11>
1037
- 1038 Michel C, Ingram RG, Harris LR. 2006. Variability in oceanographic and ecological processes
1039 in the Canadian Arctic Archipelago. *Progr Oceanogr* 71(2–4): 379–401.
1040 <https://doi.org/10.1016/j.pocean.2006.09.006>
1041
- 1042 Miller LA, Fripiat F, Else B, Bowman JS, Brown KA et al. 2015. Methods for biogeochemical
1043 studies of sea ice: The state of the art, caveats, and recommendations. *Elem Sci Anth* 3: 000038.
1044 <https://doi.org/10.12952/journal.elementa.000038>
1045
- 1046 Morel A, Smith RC. 1974. Relation between total quanta and total energy for aquatic
1047 photosynthesis. *Limnol Oceanogr* 19: 591–600.
1048
- 1049 Morozov EG, Paka VT. 2010. Internal waves in a high-latitude region. *Oceanology* 50(5): 668–
1050 674. Available at: <http://link.springer.com/10.1134/S0001437010050048>.
1051
- 1052 Münchow A, KK Falkner, H Melling. 2015. Baffin Island and West Greenland Current Systems
1053 in northern Baffin Bay. *Progr Oceanogr* 132: 305–317. ISSN 0079-6611, [doi:](https://doi.org/10.1016/j.pocean.2014.04.001)
1054 [10.1016/j.pocean.2014.04.001](https://doi.org/10.1016/j.pocean.2014.04.001).
1055
- 1056 Mundy CJ, Barber DG, Michel C. 2005. Variability of snow and ice thermal, physical and
1057 optical properties pertinent to sea ice algae biomass during spring. *J Mar Syst* 58: 107–120.
1058 <https://doi.org/10.1016/j.jmarsys.2005.07.003>
1059
- 1060 Mundy CJ, Ehn JK, Barber DG, Michel C. 2007. Influence of snow cover and algae on the
1061 spectral dependence of transmitted irradiance through Arctic landfast first-year sea ice. *J*
1062 *Geophys Res* 112: C03007. <https://doi.org/10.1029/2006JC003683>
1063

- 1064 Mundy CJ, Gosselin M, Ehn J, Gratton Y, Rossnagel A, et al. 2009. Contribution of under-ice
1065 primary production to an ice-edge upwelling phytoplankton bloom in the Canadian Beaufort
1066 Sea. *Geophys Res Lett* 36(17). ISSN 0094-8276. <https://doi.org/10.1029/2009GL038837>
1067
- 1068 Mundy CJ, Gosselin M, Gratton Y, Brown K et al. 2014. Role of environmental factors on
1069 phytoplankton bloom initiation under landfast sea ice in Resolute Passage, Canada. *Mar Ecol*
1070 *Prog Ser* 497: 39–49. <https://doi.org/10.3354/meps10587>
1071
- 1072 Newton R, Schlosser P, Mortlock R, Swift J, MacDonald R. 2013. Canadian Basin freshwater
1073 sources and changes: Results from the 2005 Arctic Ocean Section. *J Geophys Res-Oceans*
1074 118(4): 2133–2154. <https://doi.org/10.1002/jgrc.20101>
1075
- 1076 Nicolaus M, Katlein C, Maslanik J, Hendricks S. 2012. Changes in Arctic sea ice result in
1077 increasing light transmittance and absorption. *Geophys Res Lett* 39: L24501.
1078 <https://doi.org/10.1029/2012GL053738>
1079
- 1080 Olsen LM, Laney SR, Duarte P, Kauko HM, Fernández-Méndez M, Mundy CJ, et al. 2017.
1081 The role of multiyear ice in the seeding of ice-algae blooms in Arctic pack ice. *J Geophys Res-*
1082 *Bioge* 122(7): 1529–1548. <https://doi.org/10.1002/2016JG003668>
1083
- 1084 Osborn TR. 1980. Estimates of the local rate of vertical diffusion from dissipation
1085 measurements. *J Phys Oceanogr* 10(1): 83–89. ISSN 0022-3670.
1086 [https://doi.org/10.1175/1520-0485\(1980\)010%3C0083:EOTLRO%3E2.0.CO;2](https://doi.org/10.1175/1520-0485(1980)010%3C0083:EOTLRO%3E2.0.CO;2)
1087
- 1088 Pawlowicz R, Beardsley B, Lentz S. 2002. Classical tidal harmonic analysis including error
1089 estimates in MATLAB using T_TIDE. *Comput Geosci* 28: 929–937.
1090 [https://doi.org/10.1016/S0098-3004\(02\)00013-4](https://doi.org/10.1016/S0098-3004(02)00013-4)
1091
- 1092 Peralta-Ferriz C, Woodgate RA. 2015. Seasonal and interannual variability of pan-Arctic
1093 surface mixed layer properties from 1979 to 2012 from hydrographic data, and the dominance
1094 of stratification for multiyear mixed layer depth shoaling. *Prog Oceanogr* 134: 19–53.
1095 <https://doi.org/10.1016/j.pocean.2014.12.005>
1096
- 1097 Perovich DK. 1989. A two-stream multilayer, spectral radiative transfer model for sea ice
1098 (No. CRREL-89-15). Cold Regions Research and Engineering Lab, Hanover NH.
1099 https://archive.org/details/DTIC_ADA212433/page/n4
1100
- 1101 Petrich C, Eicken H. 2010. Growth, Structure and Properties of Sea Ice. In Thomas DN,
1102 Dieckmann GS, eds, *Sea Ice – An Introduction to its Physics, Chemistry, Biology and Geology*,
1103 Second Edition. Oxford: Blackwell Science Ltd, pp 23–77.

- 1104
- 1
2 1105 Petrich C, Eicken H. 2017. Overview of sea ice growth and properties. In Thomas DN ed, Sea
3 1106 Ice, 3rd Edition. John Wiley & Sons, Ltd, pp 1–41. <https://doi.org/10.1002/9781118778371.ch1>
4
5 1107
- 6
7 1108 Pineault S, Tremblay JE, Gosselin M, Thomas H, Shadwick E. 2013. The isotopic signature of
8 1109 particulate organic C and N in bottom ice: Key influencing factors and applications for tracing
9 1110 the fate of ice-algae in the Arctic Ocean. *J Geophys Res-Oceans* 118: 287–300.
10 1111 <https://doi.org/doi:10.1029/2012JC008331>
11
12 1112
- 13
14 1113 Post E, Bhatt US, Bitz CM, Brodie JF, Fulton TL et al. 2013. Ecological consequences of sea-
15 1114 ice decline. *Science* 341: 519–525. <https://doi.org/10.1126/science.1235225>
16
17 1115
- 18
19 1116 Randelhoff A, Fer I, Sundfjord A, Tremblay JÉ, Reigstad M. 2016. Vertical fluxes of nitrate in
20 1117 the seasonal nitracline of the Atlantic sector of the Arctic Ocean. *J Geophys Res-Oceans* 121(7):
21 1118 5282–5295. ISSN 2169-9291. <https://doi.org/10.1002/2016JC011779>
22
23 1119
- 24
25 1120 Randelhoff A, Fer I, Sundfjord, A. 2017. Turbulent upper-ocean mixing affected by meltwater
26 1121 layers during Arctic summer. *J Phys Oceanogr* 47(4): 835–853. [https://doi.org/10.1175/JPO-](https://doi.org/10.1175/JPO-D-16-0200.1)
27 1122 [D-16-0200.1](https://doi.org/10.1175/JPO-D-16-0200.1)
28
29 1123
- 30
31 1124 Randelhoff, A., Oziel, L., Massicotte, P., Bécu, G., Galí, M., Lacour, L., Dumont, D., Vladoiu,
32 1125 A., Marec, C., Bruyant, F., Houssais, M.-N., Tremblay, J.-É., Deslongchamps, G. and Babin,
33 1126 M., 2019. The evolution of light and vertical mixing across a phytoplankton ice-edge bloom.
34 1127 *Elem Sci Anth*, 7(1), p.20. DOI: <http://doi.org/10.1525/elementa.357>
35
36 1128
- 37
38
39 1129 Ras J, Uitz J, Claustre H. 2008. Spatial variability of phytoplankton pigment distributions in
40 1130 the Subtropical South Pacific Ocean: comparison between in situ and modelled data.
41 1131 *Biogeosciences* 5: 353–369. <https://doi.org/10.5194/bg-5-353-2008>
42
43 1132
- 44
45 1133 Ricchiazzi P, Yang SR, Gautier C, Sowle D. 1998. SBDART: a research and teaching
46 1134 software tool for plane-parallel radiative transfer in the Earth atmosphere. *B Am Meteorol Soc*
47 1135 79: 2101–2114. [https://doi.org/10.1175/1520-](https://doi.org/10.1175/1520-0477(1998)079%3C2101:SARATS%3E2.0.CO;2)
48 1136 [0477\(1998\)079%3C2101:SARATS%3E2.0.CO;2](https://doi.org/10.1175/1520-0477(1998)079%3C2101:SARATS%3E2.0.CO;2)
49
50 1137
- 51
52 1138 Riebesell U. 1989. Comparison of sinking and sedimentation rate measurements in a diatom
53 1139 winter/spring bloom. *Mar Ecol Prog Ser* 54: 109–119. <https://doi.org/10.3354/meps054109>
54
55 1140
- 56
57 1141 Ruddick B, Anis A, Thompson K. 2000. Maximum Likelihood Spectral Fitting: The Bachelor
58 1142 Spectrum. *J Atmos Ocean Tech* 17: 1541–1555. [https://doi.org/10.1175/1520-](https://doi.org/10.1175/1520-0426(2000)017%3C1541:MLSFTB%3E2.0.CO;2)
59 1143 [0426\(2000\)017%3C1541:MLSFTB%3E2.0.CO;2](https://doi.org/10.1175/1520-0426(2000)017%3C1541:MLSFTB%3E2.0.CO;2)
60
61
62
63
64
65

- 1144
- 1
2 1145 Selz V, Saenz BT, van Dijken GL, Arrigo KR. 2018. Drivers of ice algal bloom variability
3 1146 between 1980 and 2015 in the Chukchi Sea. *J Geophys Res-Oceans* 123(10): 7037–7052
4 1147 <https://doi.org/10.1029/2018JC014123>
5
6 1148
- 7
8 1149 Serreze MC, Meier WN. 2019. The Arctic's sea ice cover: trends, variability, predictability,
9 1150 and comparisons to the Antarctic. *Ann NY Acad Sci* 1436(1): 36–53.
10 1151 <https://doi.org/10.1111/nyas.13856>
11
12 1152
- 13
14 1153 Søreide JE, Leu E, Berge J, Graeve M, Falk-Petersen S. 2010. Timing of blooms, algal food
15 1154 quality and *Calanus glacialis* reproduction and growth in a changing Arctic. *Glob Change Biol*
16 1155 16(11): 3154–3163. <https://doi.org/10.1111/j.1365-2486.2010.02175.x>
17
18 1156
- 19
20 1157 Spreen G, Kaleschke L, Heygster G. 2008. Sea ice remote sensing using AMSR-E 89-GHz
21 1158 channels. *J Geophys Res* 113(C2): C02S03. Available at: <http://doi.org/10.1029/2005JC003384>
22
23 1159
- 24
25 1160 Steele DJ, Franklin DJ, Underwood GJC. 2014. Protection of cells from salinity stress by
26 1161 extracellular polymeric substances in diatom biofilms. *Biofouling* 30:8: 987–998.
27 1162 <https://doi.org/10.1080/08927014.2014.960859>
28
29 1163
- 30
31 1164 Stroeve J, Notz D. 2018. Changing state of Arctic sea ice across all seasons. *Environ Res Lett*
32 1165 13(10): 103001. Available at: <https://doi.org/10.1088/1748-9326/aade56>
33
34 1166
- 35
36 1167 Tang CL, Ross CK, Yao T, Petrie B, DeTracy BM, Dunlap E. 2004. The circulation, water
37 1168 masses and sea-ice of Baffin Bay. *Progr Oceanogr* 63(4): 183–228.
38 1169 <https://doi.org/10.1016/j.pocean.2004.09.005>
39
40 1170
- 41
42 1171 Torstensson A, Young JN, Carlson LT, Ingalls AE, Deming JW. 2019. Use of exogenous
43 1172 glycine betaine and its precursor choline as osmoprotectants in Antarctic sea-ice diatoms. *J*
44 1173 *Phycol* 55(3): 663–675. <https://doi.org/10.1111/jpy.12839>
45
46 1174
- 47
48 1175 Tremblay J-É, Anderson LG, Matrai P, Coupel P, Bélanger S, et al. 2015. Global and regional
49 1176 drivers of nutrient supply, primary production and CO₂ drawdown in the changing Arctic
50 1177 Ocean. *Progr Oceanogr* 139: 171–196. ISSN 0079-6611.
51 1178 <https://doi.org/10.1016/j.pocean.2015.08.009>
52
53 1179
- 54
55 1180 van Leeuwe MA, Tedesco L, Arrigo KR, Assmy P, Campbell et al. 2018. Microalgal
56 1181 community structure and primary production in Arctic and Antarctic sea ice: A synthesis. *Elem*
57 1182 *Sci Anth* 6: 4. <https://doi.org/10.1525/elementa.267>
58
59
60
61
62
63
64
65

1183

1 1184 Verin G, Dominé F, Picard G, Arnaud L, Babin M. 2019. Metamorphism of Arctic marine snow
 2 1185 during the melt season: Impact on albedo. *The Cryosphere* (in review).

1186

6 1187 Wassmann P, Reigstad M. 2011. Future Arctic Ocean seasonal ice zones and implications for
 7 1188 pelagic-benthic coupling. *Oceanography* 24: 220–231.
 9 1189 <https://doi.org/10.5670/oceanog.2011.74>

1190

12 1191 Wu Y, Tang C, Hannah C. 2012. The circulation of eastern Canadian seas. *Progr Oceanogr*
 13 1192 106: 28–48. <https://doi.org/10.1016/j.pocean.2012.06.005>

1193

17 1194 Contributions

19 1195 L.O. and M.B. led the design of the study. Most of the data were formatted by P.M. L.O. led
 20 1196 the writing, to which P.M and A.R. contributed. L.O. led the analysis and made the figures with
 21 1197 contributions from P.M., A.R., L.L, and A.V. M-H.F. and J.F. led the sampling. J.F. provided
 22 1198 continuous help for gathering the data. A.V. and D.D led sampling of the SCAMP data. Y.C.,
 23 1199 D.D. and P.B-A. helped in the interpretation of the ADCP and SCAMP data. P.M. and S.L-G.
 24 1200 contributed to the light section such as the processing of the PAR, the transmittance, and the
 25 1201 ice algal attenuation. All authors revised the earlier version of the manuscript, helped in the
 26 1202 interpretation and approved the final version for publication.

30 1203 Acknowledgments

31 1204 This project would not have been possible without the support of the Hamlet of Qikiqtarjuaq
 32 1205 and the members of the community as well as the Inuksuit School and its Principal Jacqueline
 33 1206 Arsenault. The community contributed to the scientific campaign by facilitating logistical
 34 1207 support and sharing local knowledge. The project is conducted under the scientific coordination
 35 1208 of the Canada Excellence Research Chair in Remote Sensing of Canada's New Arctic frontier
 36 1209 and the CNRS and Université Laval Takuvik Joint International laboratory (UMI3376). We
 37 1210 thank Françoise Pinczon du Sel and Eric Brossier from Vagabond for assistance in the field and
 38 1211 Yves Christen for fixing our valuable snowmobiles. We also thank Guislain Bécu (Takuvik),
 39 1212 Pascal Guillot (UQAR-ISMER), Shawn Mederic (Amundsen Science) for the data processing
 40 1213 and quality control of the C-OPS, CTD and ADCP respectively. We thank Caroline Sévigny
 41 1214 for deploying the SCAMP, José Luis Lagunas for deploying the ADCP, and Christian Haas for
 42 1215 sharing the time-lapse pictures of the study site area. The field campaign was successful thanks
 43 1216 to the contribution of F. Bruyant, J. Larivière, E. Rehm, C. Aubry, C. Lalande, A. LeBaron, C.
 44 1217 Marty, J. Sansoulet, D. Christiansen-Stowe, A. Wells, M. Benoît-Gagné, and E. Devred from
 45 1218 the Takuvik laboratory. We also thank Michel Gosselin, Québec-Océan, the
 46 1219 CCGS *Amundsen* and the Polar Continental Shelf Program for their in-kind contribution in
 47 1220 polar logistic and scientific equipment. We thank all participants in the Green Edge campaign
 48 1221 for their contribution to the field work and data collection.

55 1222 Funding information

57 1223 The Green Edge project is funded by the following French and Canadian programs and
 58 1224 agencies: ANR (Contract #111112), CNES (project #131425), IPEV (project #1164), CSA,
 59 1225 Fondation Total, ArcticNet, LEFE and the French Arctic Initiative (Green Edge project). L.

1226 Oziel's postdoctoral fellowship is funded by an NSERC/CRSNG 'Visiting Fellowship' in a
1227 Canadian Laboratory (DFO) and supported by the joint Laboratory Takuvik, The Canada
1228 Excellence Research Chair in remote sensing of Canada's new Arctic Frontier. S.L. Girard was
1229 supported by a postdoctoral fellowship from NSERC/CRSNG. D. Dumont is funded by a
1230 NSERC Discovery Grant 402257-2013. This work was also supported by MEOPAR
1231 through its Observation Core.

1232

1233 Competing interests

1234 The authors declare that they have no competing interests.

1235

1236 Supplemental material

1237 All references to the supplemental material have a "S" prefix.

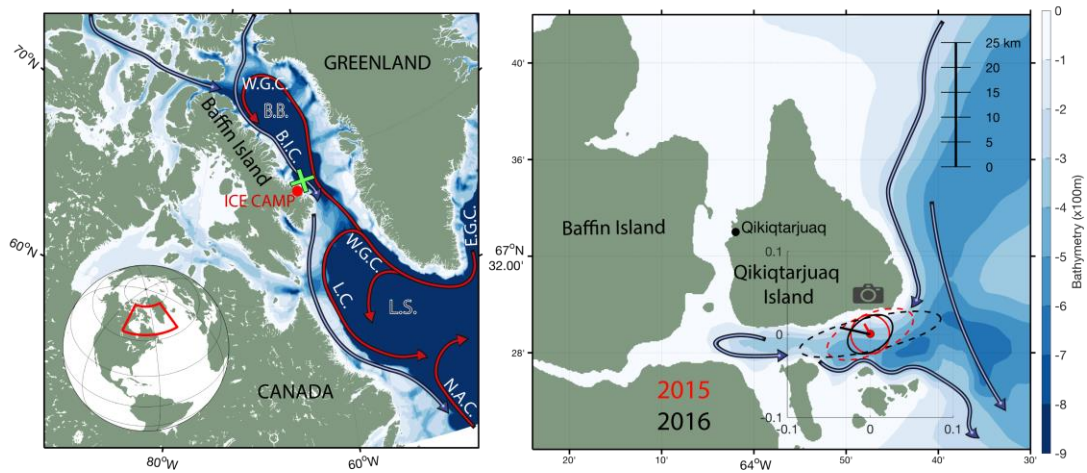
1238

1239 Data accessibility statement

1240 All data are accessible at the Green Edge database ([http://www.obs-](http://www.obs-vlfr.fr/proof/php/GREENEDGE/greenedge.php)
1241 [vlfr.fr/proof/php/GREENEDGE/greenedge.php](http://www.obs-vlfr.fr/proof/php/GREENEDGE/greenedge.php)) and will be made public after publication.

1242

1243 Figures

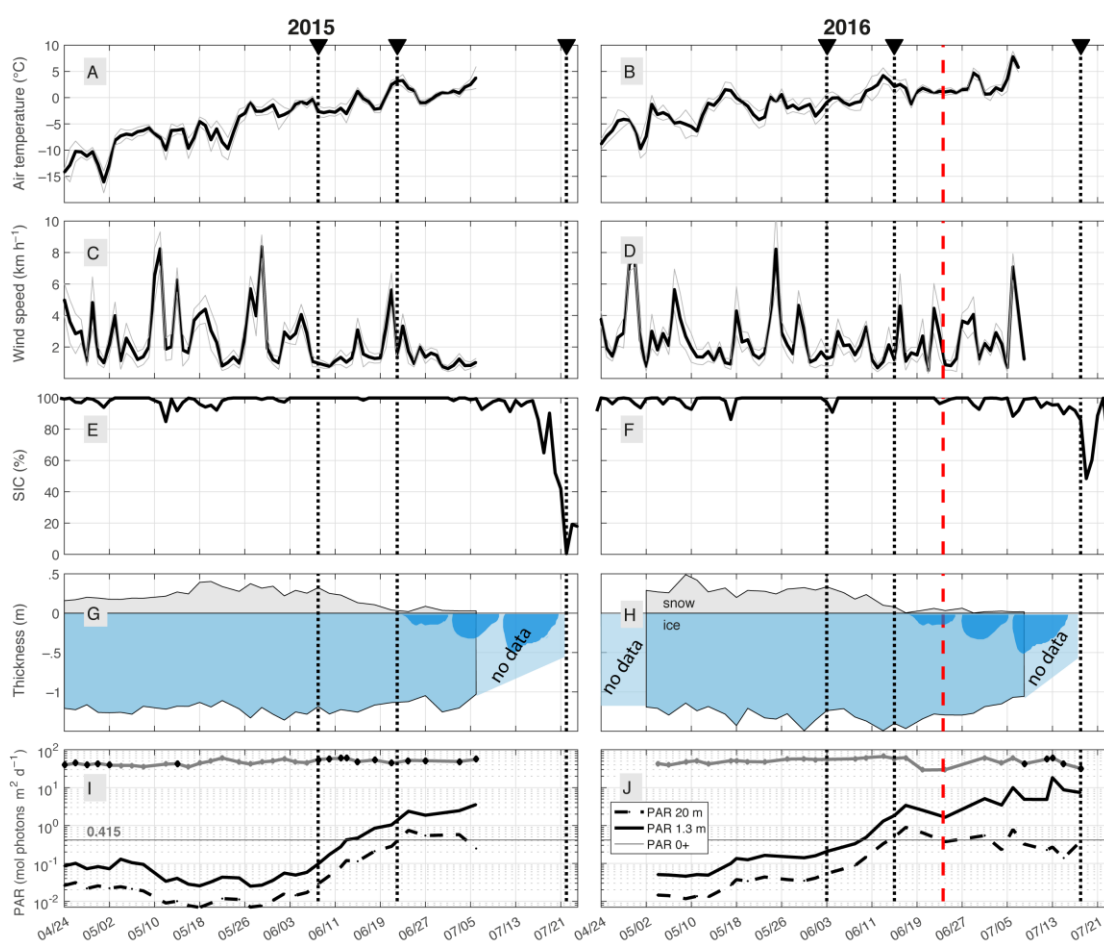


1244

1245 **Figure 1. Maps of Baffin Bay, surrounding seas and study site.** Baffin Bay and its general
 1246 surface circulation in the Eastern Canadian Arctic Ocean under Atlantic (red) or Pacific (blue)
 1247 water influence. The study site (ICE CAMP), south of Qikiqtarjuaq Island, is indicated by a red
 1248 dot. The green cross indicates station 403, the nearest station sampled by the CCGS *Amundsen*
 1249 off the continental slope in 2016. Dashed and solid lines represent the variance ellipses of the
 1250 predicted tidal currents and the daily mean velocities (m s^{-1}), respectively. The arrows show
 1251 the direction and magnitude of the mean velocity fields at 10 m over the full period (2015 in
 1252 black, 2016 in red). The camera pictogram indicates the position where the time-lapse pictures
 1253 were taken. Abbreviations: Baffin Island Current (B.I.C), Baffin Bay (B.B.), East Greenland
 1254 Current (E.G.C), Labrador Current (L.C.), Labrador Sea (L.S), North Atlantic Current (NAC),
 1255 West Greenland Current (WGC).

1256

1257



1258

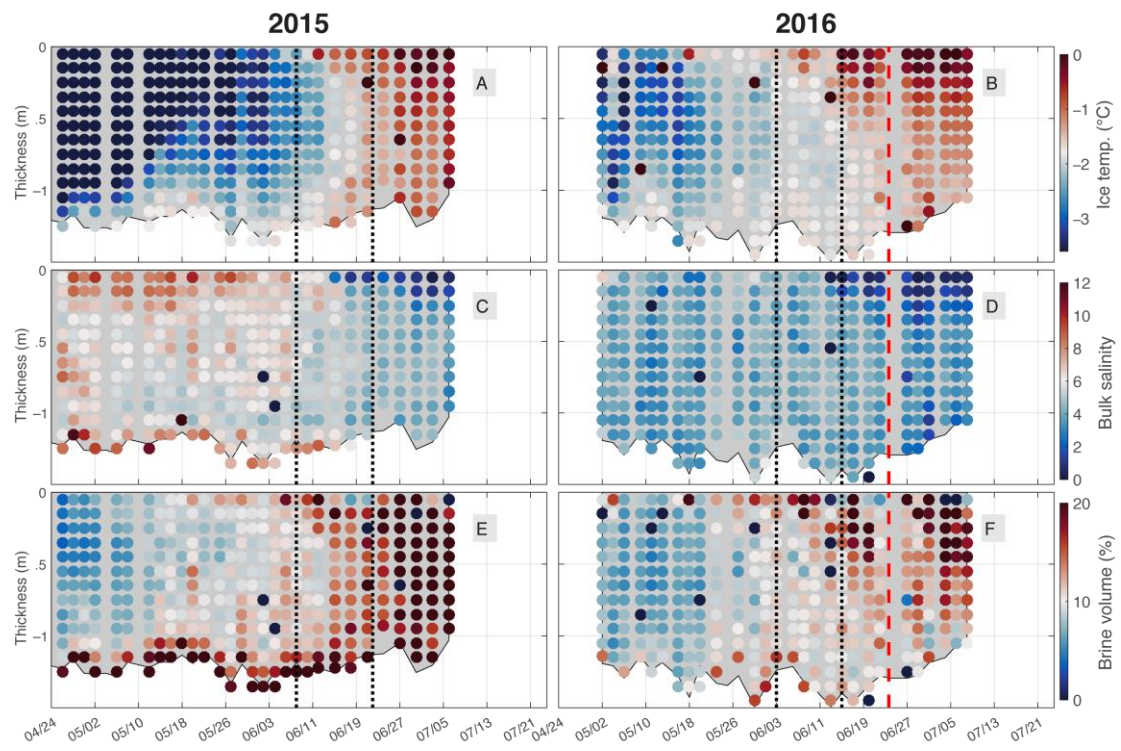
1259 **Figure 2. Temporal evolution of the environmental conditions in the air-snow-ice-ocean**
 1260 **system.** Time series of daily averaged environmental conditions for 2015 (left) and 2016 (right)
 1261 of **A, B:** air temperature ($^{\circ}\text{C}$) and **C, D:** wind speed (km h^{-1}) from the meteorological station
 1262 with standard deviation in gray; **E, F:** remotely sensed sea ice concentration (%) from the
 1263 AMSR-2 satellite; **G, H:** in situ snow and sea ice thickness (m), with melt ponds qualitatively
 1264 illustrated in deep blue; **I, J:** in situ $\text{PAR}(0+)$ above surface in gray with modeled values in
 1265 black dots, underwater PAR at 1.3 m in black solid line, and at 20 m in dashed black line.
 1266 Horizontal thin lines represent the 0.415 isolume thresholds from Letelier et al. (2004). Data in
 1267 **G, H, I** and **K** are collected at the center of the sampling circle of 1.2-km radius every 2–3 days.
 1268 Vertical dotted lines with triangle indicators on top chronologically represent snow melt
 1269 initiation, melt pond initiation and sea ice breakup. The red dashed line indicates the date when
 1270 turbulence was measured over a 13-h period. Dates are month/day.

1271

1272

1273

1274



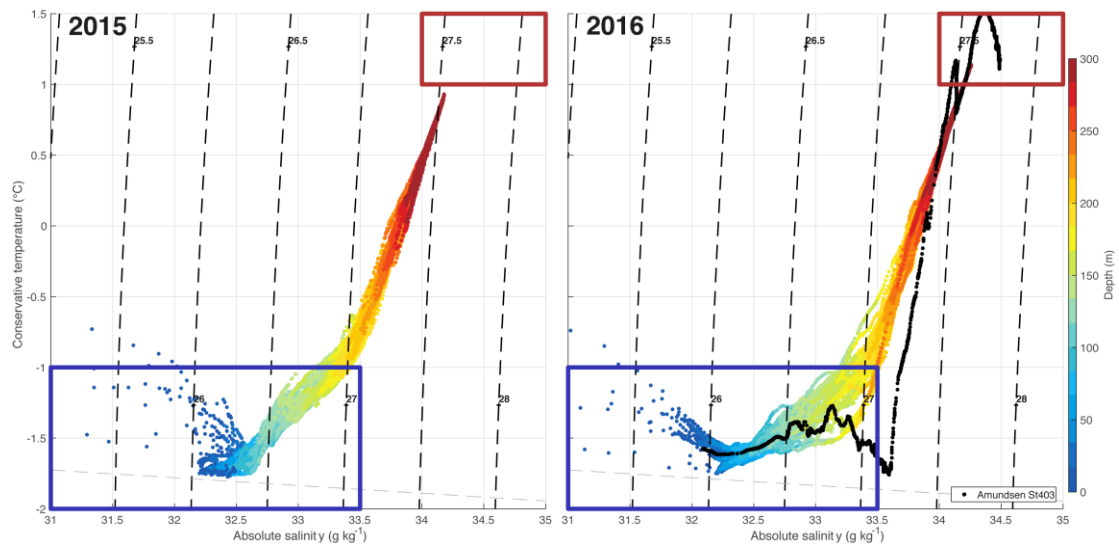
1275

1276 **Figure 3. Temporal evolution of sea ice properties.** Time series for 2015 (left) and 2016
 1277 (right) of **A, B:** sea ice temperature; **C, D:** bulk salinity; and **E, F:** brine volumes as a function
 1278 of depth (with sea ice thickness in light grey background). Vertical dotted lines chronologically
 1279 represent snow melt initiation and melt pond initiation. The red dashed line indicates the date
 1280 when turbulence was measured over a 13-h period. Dates are month/day.

1281

1282

1283



1284

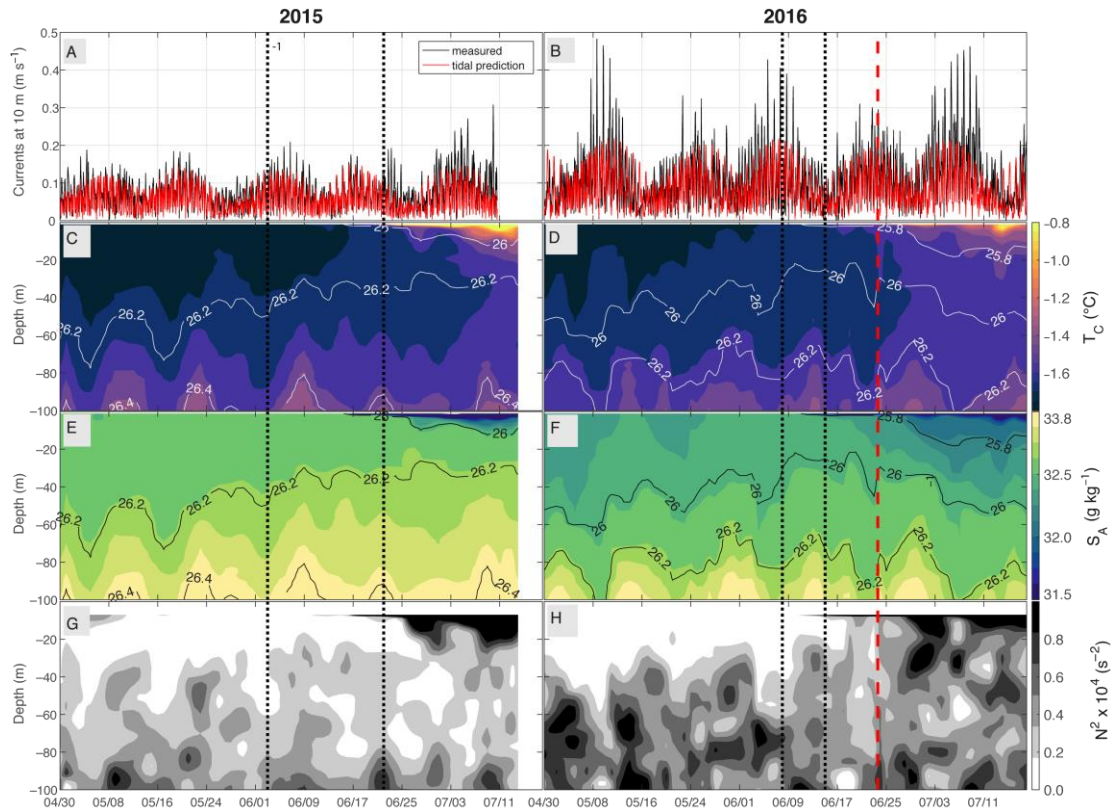
1285

1286 **Figure 4. Water masses determined from salinity, temperature and depth.** Conservative
 1287 temperature (°C) versus absolute salinity (g kg⁻¹) diagrams for all CTD profiles collected during
 1288 both 2015 (left) and 2016 (right) field campaigns. Points are colored according to depth. In
 1289 2016, the closest station (station 403; see the green cross in Figure 1) sampled by the CCGS
 1290 *Amundsen* off the continental shelf in the Baffin Bay basin is in black. The blue box defines the
 1291 Arctic Waters (AW), and the red box marks the Atlantic Waters (ArW).

1292

1293

1294



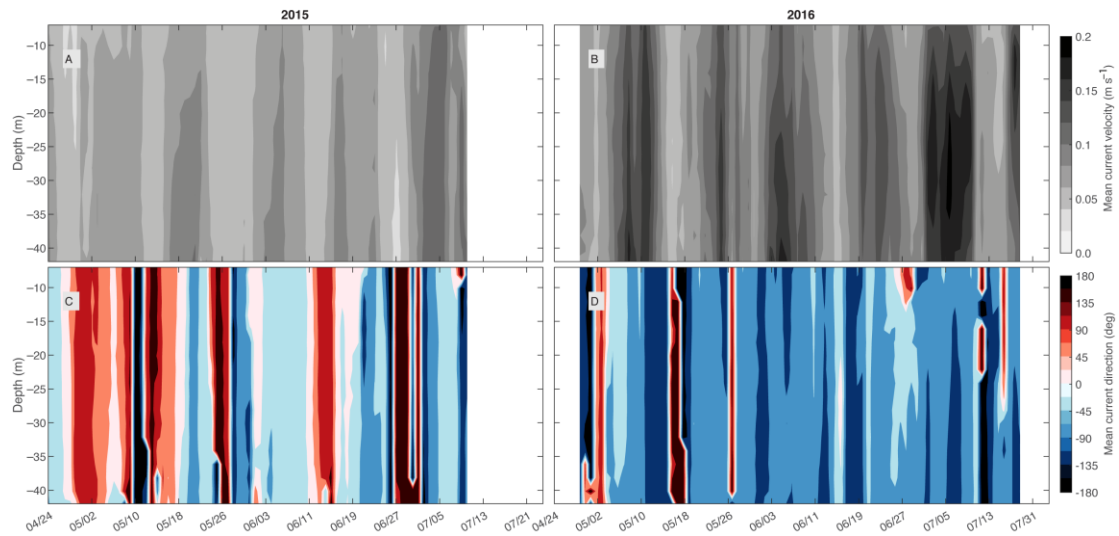
1295

1296 **Figure 5. Hydrographic temporal evolution of the water column.** Time series for the years
 1297 2015 (left) and 2016 (right) of **A, B**: in situ absolute current velocities at 10-m depth in black
 1298 and predicted from a harmonic analysis in red; **C, D**: conservative temperature Θ ($^{\circ}\text{C}$) and **E,**
 1299 **F**: absolute salinity S_A (g kg^{-1}) fields (color bars), with superimposed isopycnals of potential
 1300 density anomaly lines; and **G, H**: Brunt-Väisälä frequency N^2 (s^{-2}), (gray-scale bar). Vertical
 1301 dotted lines chronologically represent snow melt initiation, melt pond initiation and sea ice
 1302 breakup. The red dashed line indicates the date when turbulence was measured over a 13-h
 1303 period. Dates are month/day.

1304

1305

1306

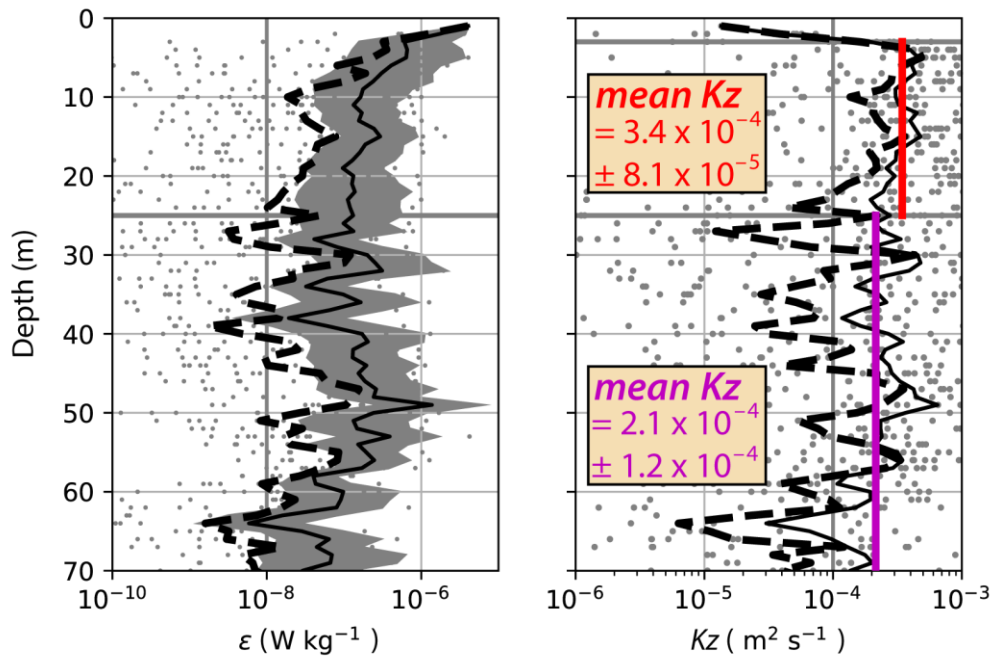


1307

1308 **Figure 6. Temporal evolution of the mean ocean current profiles.** Time series for 2015 (left)
 1309 and 2016 (right) of daily mean of **A, B:** current velocity (m s^{-1} , grey-scale bar); and **C, D:**
 1310 current direction (0° = northward, color bar). Red indicates an out-fjord/eastward direction,
 1311 while blue represents an in-fjord/westward direction. Dates are month/day.

1312

1313

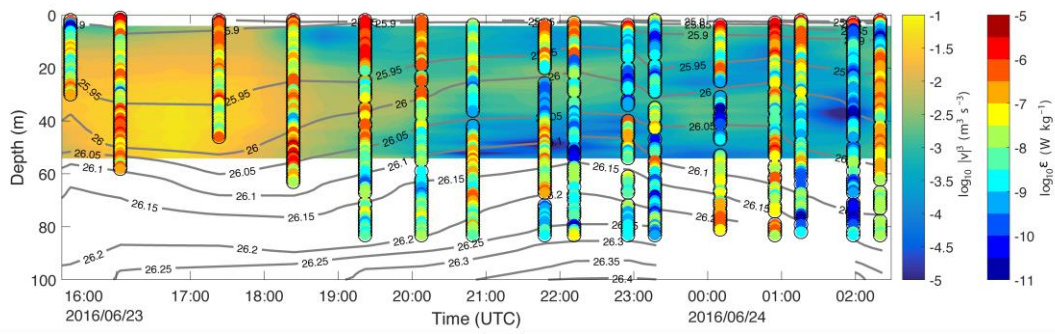


1314

1315 **Figure 7. Averaged turbulence profile during a tidal cycle.** Time-averaged mean (thin, solid)
 1316 and median (thick, dashed) dissipation rate of turbulent kinetic energy (ϵ) on the left and time-
 1317 averaged mean (thin, solid) and median (thick, dashed) vertical turbulent diffusivity (K_z) on the
 1318 right, sampled using the SCAMP during a 13-h period over a tidal cycle in 2016. The grey
 1319 shading indicates the 95% confidence limits (calculated as $\|\epsilon\| \pm 1.96\sigma/\sqrt{n}$, where σ is the
 1320 standard deviation of the log-transformed data and n is the number of samples in each bin) and
 1321 the grey dots are all data points. Insets in the right panel provide the mean K_z as arithmetic
 1322 means of the overall data points in the two indicated depth intervals, plus/minus one standard
 1323 deviation.

1324

1325



1326

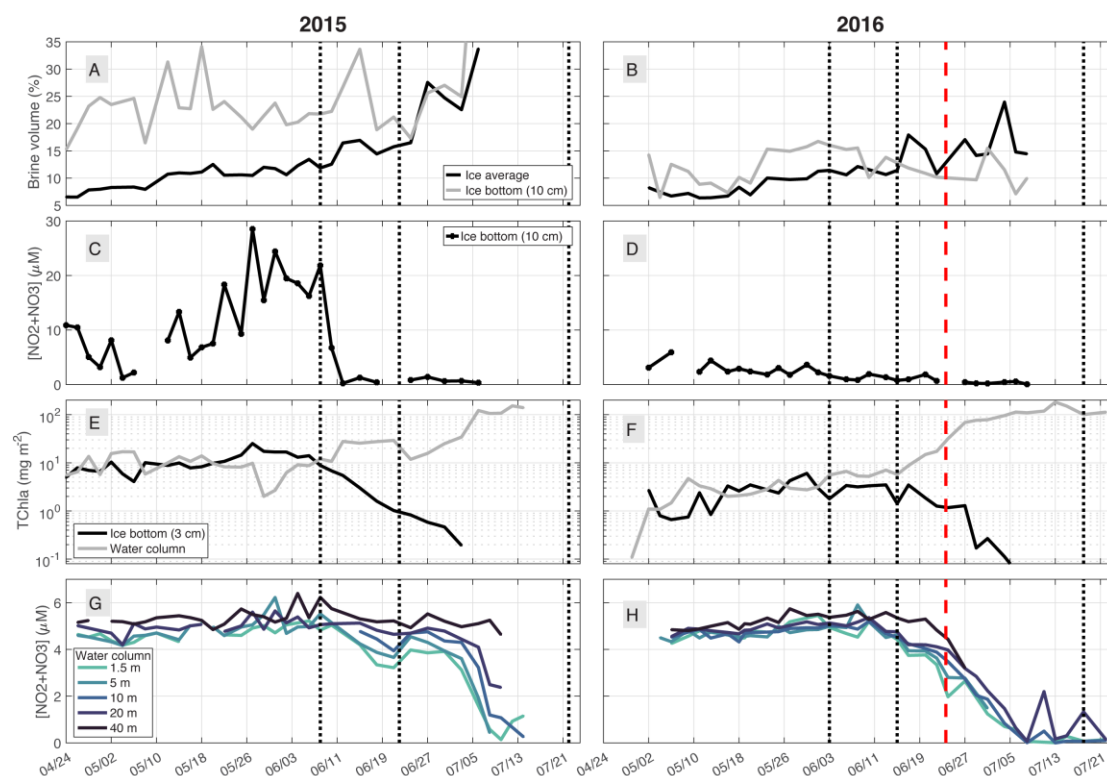
1327

1328 **Figure 8. Turbulence modulation during a tidal cycle.** The 13-h period documenting the
 1329 cubed current speed ($\text{m}^3 \text{s}^{-3}$, background field, inner color bar), and the dissipation rate of
 1330 turbulent kinetic energy (W kg^{-1} , scatter points, outer color bar) with superimposed isopycnals
 1331 of the potential density anomaly (kg m^{-3}) during a tidal cycle. Date is year/month/day.

1332

1333

1334



1335

1336 **Figure 9. Temporal evolution of biogeochemical properties in sea ice and seawater.** Time
 1337 series for 2015 (left) and 2016 (right) of **A, B:** depth-averaged and bottom sea ice brine
 1338 volumes; **C, D:** nitrate and nitrite concentration $[\text{NO}_3^- + \text{NO}_2^-]$ in the bottom 0–10 cm of the
 1339 sea ice; **E, F:** integrated TChla_{0–3cm} concentration in the bottom 0–3 cm of the sea ice in black
 1340 and in the water column in gray (note the log scale); and **G, H:** $[\text{NO}_3^- + \text{NO}_2^-]$ in the water
 1341 column at several depths. Vertical dotted lines chronologically represent snow melt initiation,
 1342 melt pond initiation and sea ice breakup. The red dashed line indicates the date when turbulence
 1343 was measured over a 13-h period. Dates are month/day.

1344

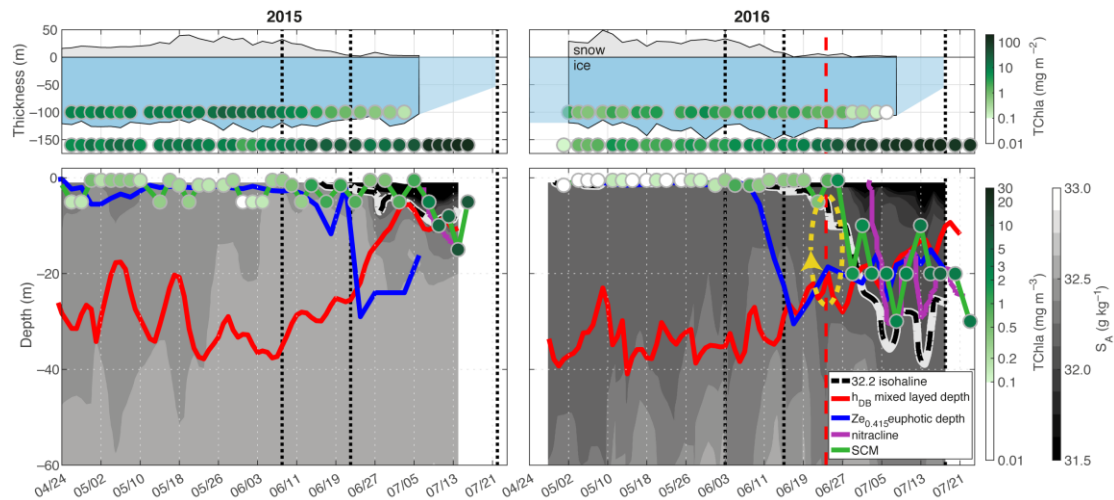


Figure 10. Representation of the algal bloom dynamics. The top panels illustrate for 2015 (left) and 2016 (right) the snow and sea ice evolution with vertically integrated ice algal (0–3 cm, blue background) and phytoplankton (surface to deepest measurement, white background) biomass in a green palette. Light blue areas correspond to periods with no data on sea ice. The bottom panels show the temporal evolution in the water column: the 32.2 isohaline, a proxy for freshwater, is a dashed black line; the equivalent mixed layer depth h_{BD} is in red; the euphotic depth $Z_{0.415}$ is represented by the isolume $0.415 \text{ mol photons m}^{-2} \text{ d}^{-1}$ in blue; the nitrate concentration of $1 \mu\text{mol L}^{-1}$ isoline (nitracline) is in magenta; the subsurface chlorophyll maximum (SCM) and corresponding $[\text{TChla}_w]$ (mg m^{-3}) are in green. The mixing layer inferred from the SCAMP sampling during a 13-h period (vertical red dashed line) is represented by the yellow arrow. Vertical dotted lines chronologically represent snow melt initiation, melt pond initiation and sea ice breakup. Dates are month/day.



Click here to access/download

Supplemental Material

OZIEL_ET_AL_ELEMENTA_SF_GREENEDGE_Supple
mental_material_v3.docx

